

PNNL-33415

Solid Phase Processing of Lead-Free Brass with Carbon Additives

September 2022

Md. Reza-E-Rabby
Abhinav Srivastava
Mayur Pole
Aditya Nittala
Bharat Gwalani
Keerti Kappagantula

DISCLAIMER

This report was prepared as an account of work sponsored by an agency of the United States Government. Neither the United States Government nor any agency thereof, nor Battelle Memorial Institute, nor any of their employees, **makes any warranty, express or implied, or assumes any legal liability or responsibility for the accuracy, completeness, or usefulness of any information, apparatus, product, or process disclosed, or represents that its use would not infringe privately owned rights.** Reference herein to any specific commercial product, process, or service by trade name, trademark, manufacturer, or otherwise does not necessarily constitute or imply its endorsement, recommendation, or favoring by the United States Government or any agency thereof, or Battelle Memorial Institute. The views and opinions of authors expressed herein do not necessarily state or reflect those of the United States Government or any agency thereof.

PACIFIC NORTHWEST NATIONAL LABORATORY
operated by
BATTELLE
for the
UNITED STATES DEPARTMENT OF ENERGY
under Contract DE-AC05-76RL01830

Printed in the United States of America

Available to DOE and DOE contractors from
the Office of Scientific and Technical
Information,
P.O. Box 62, Oak Ridge, TN 37831-0062
www.osti.gov
ph: (865) 576-8401
fox: (865) 576-5728
email: reports@osti.gov

Available to the public from the National Technical Information Service
5301 Shawnee Rd., Alexandria, VA 22312
ph: (800) 553-NTIS (6847)
or (703) 605-6000
email: info@ntis.gov
Online ordering: <http://www.ntis.gov>

Solid Phase Processing of Lead-Free Brass with Carbon Additives

September 2022

Md. Reza-E-Rabby
Abhinav Srivastava
Mayur Pole
Aditya Nittala
Bharat Gwalani
Keerti Kappagantula

Prepared for
the U.S. Department of Energy
under Contract DE-AC05-76RL01830

Pacific Northwest National Laboratory
Richland, Washington 99354

Abstract

Currently, “lead-free” brass alloys (like C27450/C27451/C6930), used extensively in drinking water fixtures and automotive, electrical, and electronic applications contain maximum 0.25% lead to maintain mechanical performance and machinability. Adding graphite to brass as an alternative to lead, using casting, powder metallurgy, and extrusion methods, has been explored previously. However, all these methods have proven to be energy-, time-, and resource-intensive, while not enabling performance equivalent to that of C36000 brass.

In this project, we developed a one-step approach using friction extrusion and ShAPE to make lead-free brass/graphite components such as wires, rods and tubes with mechanical performance equivalent to commercial lead-free brass alloys. Manufacturing temperatures were maintained ~550-730 °C with feed rates ranging between 4 – 25 mm/min. Results show larger grains at the center of the rods and wires with smaller grains developing at the edges. Graphite particles were sheared in the direction of extrusion with higher strains observed towards the edges. Hardness of the brass/graphite samples was over 25% higher than that of the corresponding brass-only samples (rods and wires), also friction extruded. Our results show that the sub-micron graphite plays an important role in limiting process temperature and restraining grain growth during friction extrusion, thus reducing grain size in composites.

Acknowledgments

Kappagantula appreciates the technical and commercial guidance for developing lead free brass rod manufacturing as well as feedstock materials for this project provided by Mueller Inc.

This research was supported by the I3T Investment, under the Laboratory Directed Research and Development (LDRD) Program at Pacific Northwest National Laboratory (PNNL). PNNL is a multi-program national laboratory operated for the U.S. Department of Energy (DOE) by Battelle Memorial Institute under Contract No. DE-AC05-76RL01830.

Contents

Abstract.....	ii
Acknowledgments.....	iii
1. Introduction.....	1
2. Materials and Methods.....	2
2.1. Materials.....	2
2.2. Lead-Free Brass Rod and Tube Synthesis.....	2
2.3. Mechanical Performance Testing.....	4
2.4. Microstructural Characterization.....	4
3. Results and Discussion.....	6
3.1. Lead-Free Brass Rods and Tubes.....	6
3.2. Mechanical Performance.....	7
3.3. Microstructural Characterization.....	12
4. Conclusions.....	21
References.....	23
Appendix A – ShAPE Process Parameters for Manufacturing Lead Free Brass Components.....	24
Appendix B – Mechanical Properties and Microstructural Images of Lead-Free Brass Components Manufactured via ShAPE.....	25

Figures

Figure 1: Shear assisted processing and extrusion equipment available at PNNL used for manufacturing lead free brass wires, rods, and tubes in this project.2

Figure 2: Schematic showing the different steps involved in the friction extrusion of lead-free brass rods.3

Figure 3: (a) Green compaction of powder around the mandrel within the liner and mandrel base, (b) ShAPE die used in this study instrumented with TC channel for temperature recording and placed in the tool holder in the spindle side of the machine, (c) chilled container with green compaction placed in the hydraulic head of ShAPE machine that has linear motion enabled.4

Figure 4: (a) Friction extruded lead-free brass rod (2.5 mm diameter) attached to die after the process, (b) rod removed from the die and cut off from billet remnant (inset), and (c) close up image of the rod.6

Figure 5: (a) Friction extruded lead-free brass rod (5 mm diameter) at different process conditions, and (b) close shot of the rods with tool mark on surface.6

Figure 6: (a) Lead-free brass tubes: 12 mm OD, 1 mm wall thickness, produced at different processing conditions, (b) maximum length of tube was 750 mm, (c) surface appearance of tube produced at 4 mm/min and 550 °C steady temperature, and (d) surface appearance of tube produced at 24 mm/min and 600 °C.7

Figure 7: Relation between friction extrusion processing temperature and microhardness obtained for the brass and brass + graphite samples. Lower is the processing temperature, higher is the hardness.9

Figure 8: Engineering stress vs strain result of Ø 5 mm friction extrusion processed brass rods.10

Figure 9: Comparison of ultimate tensile stress (UTS), yield strength (YS), and %elongation in different friction extruded rods with different brass rods from Mueller Brass Co.10

Figure 10: Hardness of (a) brass-only and (b) brass/graphite friction extruded wires; (c). stress-strain behavior of the brass samples manufactured in this project.11

Figure 11: SEM and EDS results of initial: (a)-(b) brass and (c)-(d) brass+graphite powders.12

Figure 12: SEM and EDS results of friction extruded Ø 5mm brass rod LFB 7. (a) and (e) show the schematic of regions on the longitudinal and transverse section respectively for SEM imaging. (b)-(d) SEM microstructure from longitudinal section. (f)-(g) SEM from transverse section. (h) EDS results showing homogenous distribution of Cu and Zn.13

Figure 13: SEM and EDS results of friction extruded Ø 5mm brass+graphite rod LFB 16. (a) and (e) show the schematic of regions on the longitudinal and transverse section respectively for SEM imaging. (b)-(d) SEM microstructure from longitudinal section. (f)-(g) SEM from transverse section. (h) EDS results showing homogenous distribution of Cu and Zn and presence of carbon sheared during friction extrusion.14

Figure 14: EBSD and KAM images of the brass/graphite friction extruded sample LFB 16 with 5-mm-diameter in the transverse section.	15
Figure 15: (a) Average grain size of friction extruded \varnothing 5mm brass and brass+graphite rods. (b) and (c) show the dependence of grain size and hardness along longitudinal and transverse direction of the rods (Hall-Petch relationship).....	15
Figure 16: Shearing of graphite particles in brass/graphite composite after friction extrusion.	16
Figure 17: SEM and EDS imaging of the front and end positions of the friction extruded brass-only wire with 2.5 mm diameter in the longitudinal and transverse directions.	17
Figure 18. SEM and EDS imaging of the front and end positions of the friction extruded bras/graphite wire with 2.5 mm diameter in the longitudinal and transverse directions.	18
Figure 19: EBSD and KAM imaging of friction extruded 2.5 mm brass/graphite wire in the traverse direction at the center and edge of the wire.	18
Figure 20: TEM results of friction extruded 2.5 mm diameter brass/graphite wire. (a) Area from where FIB lift out was performed. (b) Bright field TEM (c) EDS of the sheared graphite region. (d) STEM image (e) STEM-EDS maps (f) Transition in the [001] zone axis of the Cu and graphite.....	19
Figure 21 SEM and EDS results of friction extruded \varnothing 5mm brass rod LFB 4. (a) and (e) show the schematic of regions on the longitudinal and transverse section respectively for SEM imaging. (b)-(d) SEM microstructure from longitudinal section. (f)-(g) SEM from transverse section.	28
Figure 22. SEM and EDS results of friction extruded \varnothing 5mm brass + graphite rod LFB 6. (a) and (e) show the schematic of regions on the longitudinal and transverse section respectively for SEM imaging. (b)-(d) SEM microstructure from longitudinal section. (f)-(g) SEM from transverse section. (h) EDS results showing homogenous distribution of Cu and Zn and presence of carbon sheared during friction extrusion.	29
Figure 23. SEM and EDS results of friction extruded \varnothing 5mm brass + graphite rod LFB 15. (a) and (e) show the schematic of regions on the longitudinal and transverse section respectively for SEM imaging. (b)-(d) SEM microstructure from longitudinal section. (f)-(g) SEM from transverse section. (h) EDS results showing homogenous distribution of Cu and Zn and presence of carbon sheared during friction extrusion.	29
Figure 24. SEM and EDS results of friction extruded \varnothing 5mm brass+graphite rod LFB 9. (a) and (e) show the schematic of regions on the longitudinal and transverse section respectively for SEM imaging. (b)-(d) SEM microstructure from longitudinal section. (f)-(g) SEM from transverse section.	30
Figure 25: SEM and EDS results of friction extruded \varnothing 5mm brass+graphite rod LFB 13. (a) and (e) show the schematic of regions on the longitudinal and transverse section respectively for SEM imaging. (b)-(d) SEM microstructure from longitudinal section. (f)-(g) SEM from transverse section. (h) EDS results showing homogenous distribution of Cu and Zn with added carbon distributed throughout.	30

Tables

Table 1: Friction extrusion processing parameters and hardness of brass-only and brass/graphite rods with 5-mm-diameter.	8
Table 2. Trials and corresponding control parameters and response variables during friction extrusions and ShAPE process	24

1. Introduction

Brasses are copper (Cu) based alloys with zinc (Zn) alloying additions; brass properties depend on the concentration of Zn. In addition to 30 – 50 wt.% Zn, other alloying additions such as silicon, tin, lead, arsenic, and nickel are also added to brasses to develop properties such as corrosion resistance, wear resistance, machinability, dezincification, tarnish resistance and stress corrosion cracking. Brasses are extensively used in a wide variety of applications ranging from springs, fire extinguishers, jewelry, radiator cores, lamp fixtures, ammunition, flexible hose and bearings owing to their high strength, ductility and cold workability.

Lead-free brass is used extensively in buildings (drinking water fixtures), automotive, electrical and electronic industries. This is a misnomer however, since currently used lead-free brass alloys (C83600 and C36000) contain less than 0.25% lead. There is a need to develop brass varieties with high strength, ductility, malleability and machinability without any lead to entirely minimize environmental interaction with the hazardous material. This is particularly critical need currently owing to the new EPA restrictions that require lead-free brass to be truly lead free by 2023.

Addition of graphite to brass was explored to enhance machinability while lowering friction coefficient under dry sliding previously (Ghorbani et al. 2001). Several manufacturing processes such as casting, powder metallurgy, and extrusion methods were used to incorporate graphite into brass substrates in the form of powder, flake or solid feedstocks (Li et al. 2016). However, all these methods have proven to be energy-, time-, and resource-intensive, while not enabling performance equivalent to that of C83600 and C36000 (Zhang et al. 2020). Common problems that arise are porosity, oxidation of substrates, phase separation and undesirable intermetallic formation. There is a clear opportunity in developing technology and capabilities on manufacturing porosity-free, brass/graphite composites with performance metrics such as machinability, tensile performance and wear resistance similar to that of 'lead-free' brass available commercially.

In this project, we developed lead free brass components such as wires, rods and tubes with graphite additions using shear assisted processing and extrusion (ShAPE™) equipment developed at PNNL. The feedstock materials, namely brass-only powders and brass/graphite powders were provided by Mueller Industries. We developed ShAPE tooling and identified process parameter windows that enabled the synthesis components with minimal surface defects. We determined the mechanical properties of the brass-only and brass/graphite composite components. We also performed microstructural imaging to identify features of interest that may be responsible for the performance development in the lead-free brass materials.

2. Materials and Methods

2.1. Materials

Materials used for this work are lead-free brass in pure form (Cu-40Zn) mixed with 7.5 wt.% graphite additives. All the materials were obtained from Mueller Bass Co., a business segment of Mueller Industries, Inc. The pre-mix powders of the lead-free brass are among the EcoStream™ family of alloys similar to previous generation C27450/ C27451/ C6930 which contained maximum 0.25% lead (Pb) to maintain mechanical performance and machinability. These specific alloys are designed for improved machinability and forgeability that comply with the regulations of the “Reduction of Lead in Drinking Water Act” to replace lead with graphite as well as adopted dezincification resistance criteria. Since no potential harmful contaminants like silicon, bismuth, arsenic and lead are added, the manufacturing scraps and post-consumer wastes of this brass alloy is easily recyclable.

2.2. Lead-Free Brass Rod and Tube Synthesis

All the friction extrusions of rods and ShAPE of tubes were performed using the ShAPE machine (Figure 1). The machine has a maximum rotational speed of 500 rpm, rotational speed of 3000 N-m, ram speed of 480 mm/min under no load, and ram force of 900 kN. The ShAPE machine is controlled by a built-in GUI that can be used to program the machine in feed rate control mode. The extrusion force, power, torque, and process temperature can also be recorded. The machine is also capable of temperature and power control extrusions for certain alloys.



Figure 1: Shear assisted processing and extrusion equipment available at PNNL used for manufacturing lead free brass wires, rods, and tubes in this project.

Two types of tooling were introduced for friction extrusion of wires having diameter of 2.5 mm and rods with 5 mm diameter. A flat face die with 25.4 mm (1.0”) outer diameter (OD) and 2.54 mm (0.1”) inner diameter (ID) was used for extruding 2.5 mm diameter wire at an extrusion ratio of 100:1.

For extruding 5 mm diameter brass rod, a scrolled face die having 31.75 mm (1.25") OD and 5 mm (0.2") ID was employed. The extrusion ratio in the case of 5 mm diameter brass rod was 39.3:1. All the dies were made of MP159 (Ni-Co-Cr based alloy) and instrumented with k-type thermocouple to record the die temperature during friction extrusion. The liner in which the powders are compacted, is made of H13 steel that were austenitized for achieve hardness HRC > 50. Figure 2 presents workflow and step-by-step procedure of extruding wires and rods using the ShAPE machine.

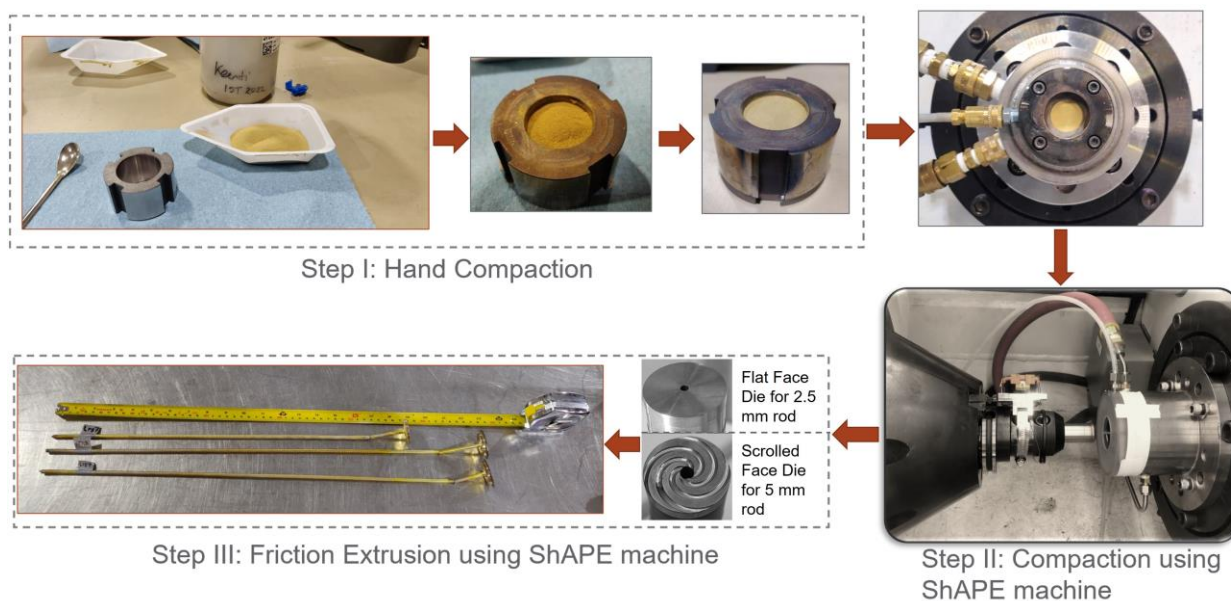


Figure 2: Schematic showing the different steps involved in the friction extrusion of lead-free brass rods.

In Step I (Figure 2), the brass powders were compacted in the designated liner using a handheld hydraulic press by applying a force of about 80 kN. This pre-compaction of loose powder is required to accommodate it in the liner (top right image of Figure 2) in the horizontal position to prevent the powder falling off from the container. In Step II, the ShAPE machine with the extrusion die was used for a final cold compaction with the machine load up to 150 kN. In Step III, the friction extrusion was performed using the rotating die feeding into the compacted powder at a constant ram speed and varying rotational speed to maintain specific die temperature. Table A in the Appendix provides the processing parameters used in this study for producing brass-only and brass/graphite wires. In essence, the feed rates are varied within 4-24 mm/min with variable rotational speed to extrude within a wide range of die temperature (450-740 °C). For the combination of extrusion parameters, both the brass-only and brass/graphite composite rods were produced using friction extrusion.

In this project, brass-only and brass/graphite tubes with a 12 mm OD and 1 mm wall thickness were also manufactured. A billet liner with 31.8 mm ID, die having 31.75 mm OD and 12 mm ID was used during manufacturing along with a 10 mm diameter mandrel. The space between the die ID and mandrel dictates the thickness of the tube which is 1 mm in this study. The detailed setup of the tooling can be found in the previous report (Whalen et al. 2021). Similar steps as shown in Figure 2 were adopted for the compaction of brass powder except that there was a centered mandrel placed before the powder compaction sequence shown in Figure 3(a). The

die and billet container mounted on the ShAPE machine were also shown in Figure 3(b-c). The two parameter sets were employed for the tube extrusions which are: (a) feed rate 4 mm/min. and die temperature 550 °C near steady condition and (b) feed rate 24 mm/min. and die temperature 600 °C near steady condition.

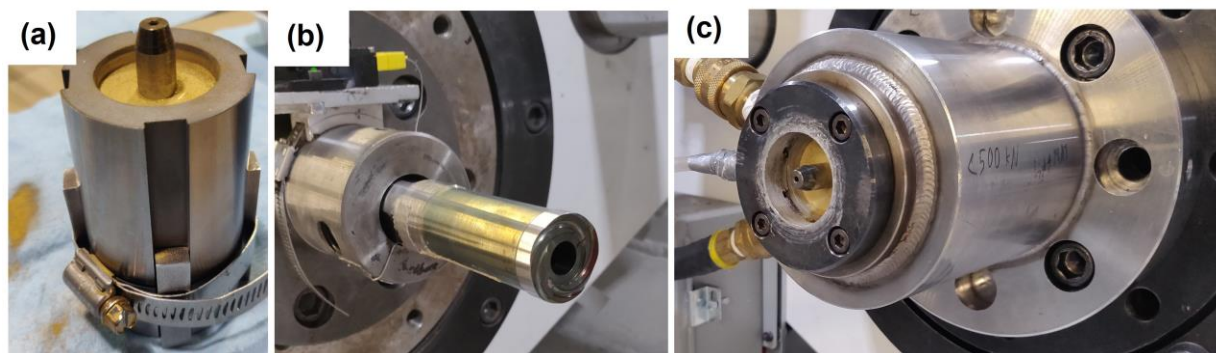


Figure 3: (a) Green compaction of powder around the mandrel within the liner and mandrel base, (b) ShAPE die used in this study instrumented with TC channel for temperature recording and placed in the tool holder in the spindle side of the machine, (c) chilled container with green compaction placed in the hydraulic head of ShAPE machine that has linear motion enabled.

2.3. Mechanical Performance Testing

The mechanical performance of friction extruded brass-only and brass/graphite wires and rods were assessed via microhardness (Vickers hardness) measurements and tensile tests. The hardness samples were taken at a distance of 10 mm away from the front end of the extrudate samples to ensure that the representative sample was obtained from the region where steady state processing conditions were applied. While the hardness measurements were taken from several locations in both the transverse and longitudinal sections for the 5 mm diameter rods, the hardness measurements were only taken along longitudinal section for the 2.5 mm diameter wires. For microhardness measurements, a load of 200 gf was applied for a dwell time of 12 s with the indentation spacing of 0.3 mm as per ASTM E384.

The room temperature tensile tests were performed on the Admet micro tensile tester at a crosshead displacement rate of 0.5 mm/min for the rods and at a rate of 1.27 mm/min for the wires. Mini tensile specimens, 38 mm long having a gage length and gage diameter of 16 mm and 3 mm respectively, were produced from the rods. On the other hand, rods of gage length of 25 mm were obtained from the 2.5 mm diameter wires, which were then used for tensile testing. At least two samples were tested from each rod or wire for repeatability.

2.4. Microstructural Characterization

For microstructural characterization, samples were obtained from both the transverse cross-section and the longitudinal section using a diamond saw from the steady-state region of the rods i.e., 10 mm away from the front end of extrusion. Subsequently, the samples were mounted in epoxy and polished to a final surface finish of 0.05 μm using colloidal silica. Both the rods and wire samples were characterized using scanning electron microscopy (SEM), backscattered electron diffraction, energy dispersive X-ray spectroscopy (EDS), and electron backscatter diffraction (EBSD). Further, the wires were characterized using the bright-field

transmission electron microscopy (BFTEM), high-resolution transmission electron microscopy (HRTEM), and selected area diffraction patterns (SADP). The sample preparation for HRTEM and APT was performed using a Thermo Fisher Scientific Quanta 200 FIB-SEM outfitted with an Oxford Instruments EDS system for compositional analysis. An FEI Titan 80–300 operated at 300 kV was used for HRTEM.

3. Results and Discussion

3.1. Lead-Free Brass Rods and Tubes

Figure 4(a) and (b) present a 2.5 mm diameter wire about 800 mm long produced via friction extrusion process. The billet remnant with wire is also shown in the inset of Figure 4(b). The top right side of Figure 4(b) provide the evidence of minor flash sticking with friction extrusion die that was expelled between the die OD and liner ID. Figure 4(b) shows the surface appearance of the segment of the rod which is straight and smooth.

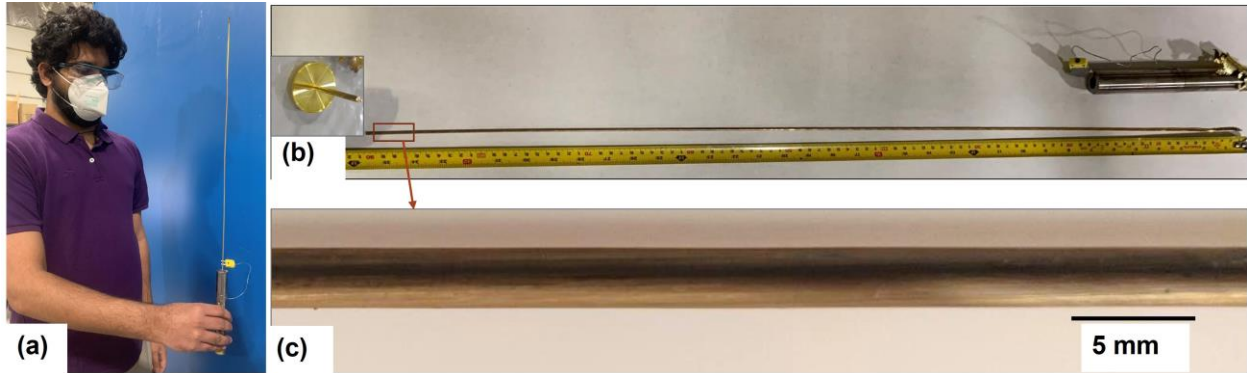


Figure 4: (a) Friction extruded lead-free brass rod (2.5 mm diameter) attached to die after the process, (b) rod removed from the die and cut off from billet remnant (inset), and (c) close up image of the rod.

Figure 5(a) presents the 5 mm diameter brass-only and brass/graphite rods extruded at different process conditions. The surface appearance in Figure 5(b) revealed tool marks (due to presence of scroll feature on die face) at low feed rate (4 mm/min) which is commonly observed in friction extrusion process. However, this tool mark disappeared with increasing feed rate to 24 mm/min.

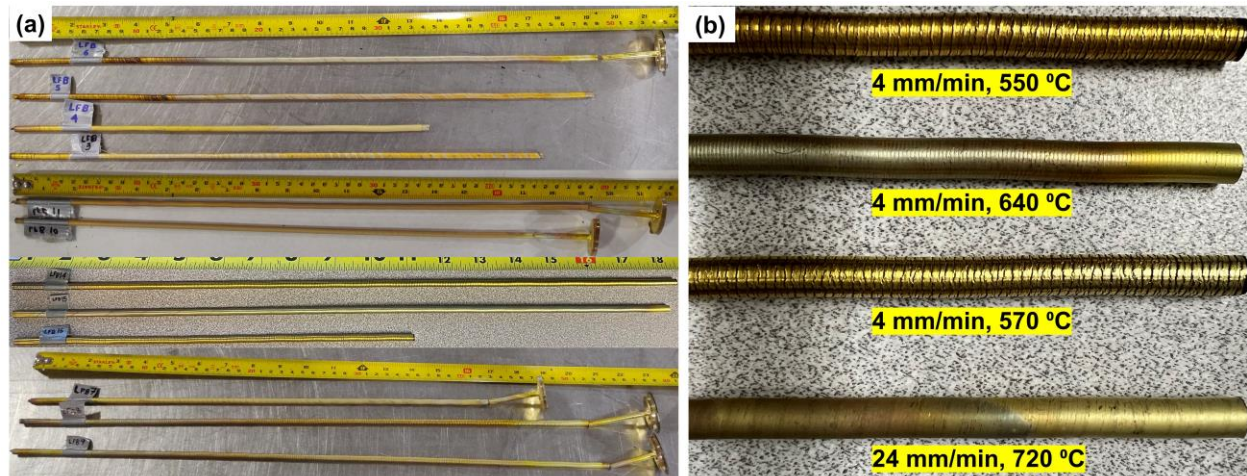


Figure 5: (a) Friction extruded lead-free brass rod (5 mm diameter) at different process conditions, and (b) close shot of the rods with tool mark on surface.

Figure 6(a-b) presents 12 mm diameter OD and 1 mm wall thickness brass/graphite tubes produced using SHAPE process. The maximum length of the extruded brass tube is 750 mm

(Figure 6-b). Two sets of parameters (4 mm/min, 550 °C and 24 mm/min, 600 °C) were repeated twice to produce 4 tubes as a proof of concept as showed in Figure 6(a). Surface appearances of lead-free brass tubes made with two different feed rate and temperature combinations illustrated in Figure 6(c) and (d). A finer pitch of the tool mark pattern can be observed in Figure 6(c) for a 4 mm/min. feed rate. However, the frequency of these tool marks decreases with increasing feed rate to 24 mm/min. as revealed in Figure 6(d). These tubes were produced as a proof-of-concept and no further analyses were made on tubes to evaluate the mechanical performance or microstructural characterization.

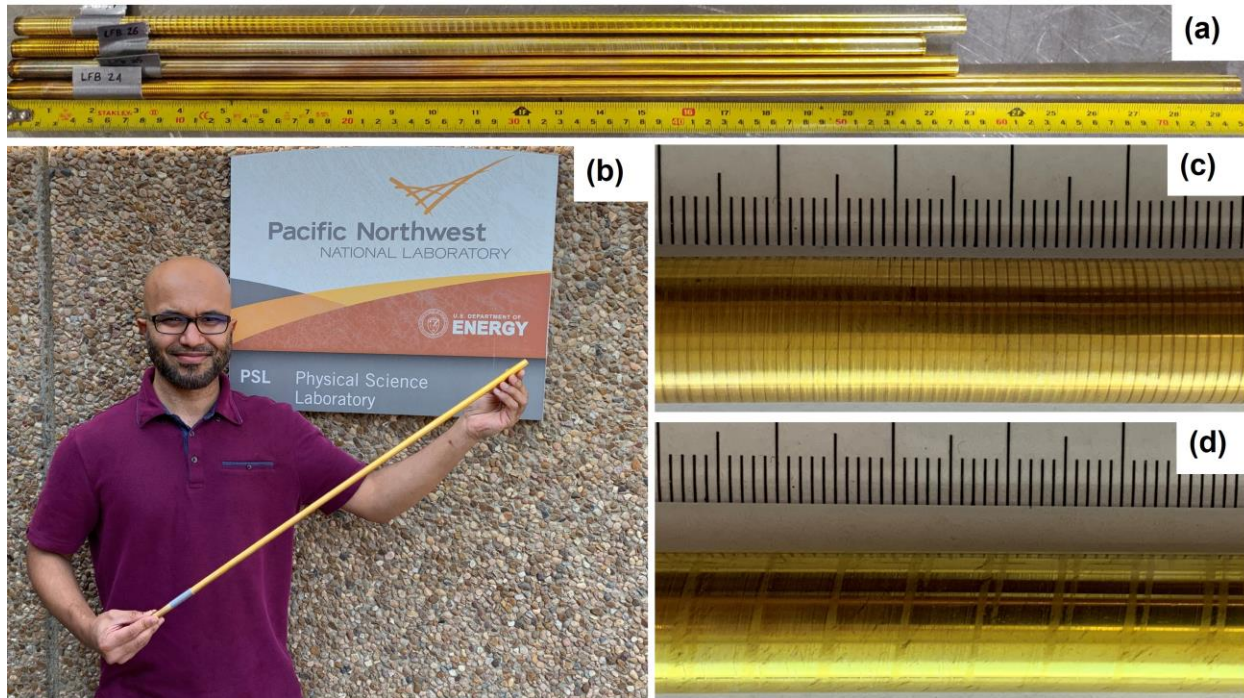


Figure 6: (a) Lead-free brass tubes: 12 mm OD, 1 mm wall thickness, produced at different processing conditions, (b) maximum length of tube was 750 mm, (c) surface appearance of tube produced at 4 mm/min and 550 °C steady temperature, and (d) surface appearance of tube produced at 24 mm/min and 600 °C.

3.2. Mechanical Performance

The average hardness of friction extruded brass-only and brass/graphite rods is presented in **Error! Reference source not found.** Appendix B shows the location from which hardness samples were obtained and a schematic shows the location of hardness indents. The friction extrusion direction is along Z-axis, whereas X and Y axes are perpendicular to it. It is evident from **Error! Reference source not found.** that all the control samples (LFB 4, LFB 7, LFB 10, LFB 17, LFB 20) have homogenous hardness distribution in both transverse and longitudinal sections. Additionally, the average hardness in most of the control samples is lower than that in the brass/graphite rods. Note the variation in hardness distribution for brass/graphite samples. We hypothesize that such a variation may be due to the use of different friction extrusion parameters to achieve optimum results.

Table 1: Friction extrusion processing parameters and hardness of brass-only and brass/graphite rods with 5-mm-diameter.

Sample ID	Sample description	Feed rate (mm/min.)	DAPR (mm/R)	Temperature (°C)	Avg. Microhardness	
					Traverse (Hv)	Longitudinal (Hv)
LFB 4	Brass-only	4-16	0.322	678	105.05 ± 1.76	102.08 ± 1.64
LFB 5	Brass/graphite	4-16	0.323	670	103.87 ± 6.74	100.98 ± 8.92
LFB 6	Brass/graphite	4-24	0.287	552	111.34 ± 9.3	111.65 ± 7.08
LFB 7	Brass-only	4-8	0.114	713	96.69 ± 2.43	97.17 ± 2.36
LFB 9	Brass/graphite	4-8	0.034	634	103.39 ± 5.31	101.38 ± 6.56
LFB 10	Brass-only	4-8	0.089	719	93.57 ± 1.1	95.14 ± 2.0
LFB 11	Brass/graphite	4-8	0.035	710	102.34 ± 3.54	100.91 ± 4.32
LFB 13	Brass/graphite	4-24	0.076	680	98.25 ± 4.89	99.5 ± 4.73
LFB 14	Brass/graphite	4	0.027	544	120.96 ± 5.63	121.01 ± 7.36
LFB 15	Brass/graphite	4	0.011	639	104.83 ± 4.21	105.68 ± 6.05
LFB 16	Brass/graphite	4	0.033	552	123.81 ± 6.47	121.02 ± 8.29
LFB 17	Brass-only	4	0.11	628	103.18 ± 1.35	102.42 ± 1.6
LFB 20	Brass-only	24	0.202	731	97.91 ± 1.08	97.35 ± 1.77

LFB 4 is the control sample for LFB 5 rod. It is observed that with the feed rate in the range of 4-16 mm/min and processing temperature of 670-680 °C, both the rods show similar hardness values and not much improvement in hardness is seen with addition of graphite. Subsequently, to improve the hardness in brass/graphite samples, the processing temperature for LFB 6 was reduced to ~550 °C and the feed rate range increased to 4-24 mm/min, this resulted in an increase in hardness to ~111 HV.

It is interesting to note that in LFB 6, the hardness in the center of the rod was lower and increased away from the center, reaching the highest value just at the rod surface. In an attempt to achieve homogenous hardness throughout the thickness and length of the rod, based on LFB 6 parameters, the temperature was increased further in LFB 13 to ~680 °C. This increase in processing temperature led to a decrease in hardness to ~99HV. Also, the inhomogeneity in the hardness was still seen in LFB 13. Next, the rods were processed at a lower feed rate of 4-8 mm/min and various temperature ranges. Results from LFB 7, 9, 10, and 11 confirmed that the rods extruded at a lower feed rate and lower temperature resulted in higher average hardness. In order to maximize hardness and therefore mechanical performance, LFB 14-16 were extruded at 4 mm/min feed rate and at a lower temperature range of ~550-650 °C. This processing condition resulted in best average hardness values greater than 120 HV and greater homogeneity in the rods as well.

Our results in this study show that as the temperature during the friction extrusion process is lowered, an increase in hardness of the brass and brass + graphite rods is observed as expected. The processing temperature of brass is $> 0.5T_m$ where T_m is the melting temperature of brass. Hence, dynamic recrystallization can be expected to occur, leading to the formation of equiaxed grains as shown in Section 3.3. When the temperature is lowered, but not below $0.5T_m$, partial recrystallization occurs. Therefore, the refined Cu-Zn grains resulting from friction extrusion processing are strained, resulting in higher hardness. Further, friction extrusion applies severe plastic deformation to the material, in turn, causing grain refinement. Therefore, the samples processed at relatively lower temperature showed bimodal grain size distribution, which is the likely cause of variation in hardness within a rod. Additionally, a lower hardness

values observed in the middle of the rod as compared to the surface could be due to the difference in cooling rate of the rods.

The evidence of dependence of hardness of the brass rods on the processing temperature is further shown in **Error! Reference source not found.** which shows that as the processing temperature is lowered, higher hardness is obtained. The hardness obtained in the present study is higher than that reported in the literature (Stoddart et al. 1979) for brasses of similar composition.

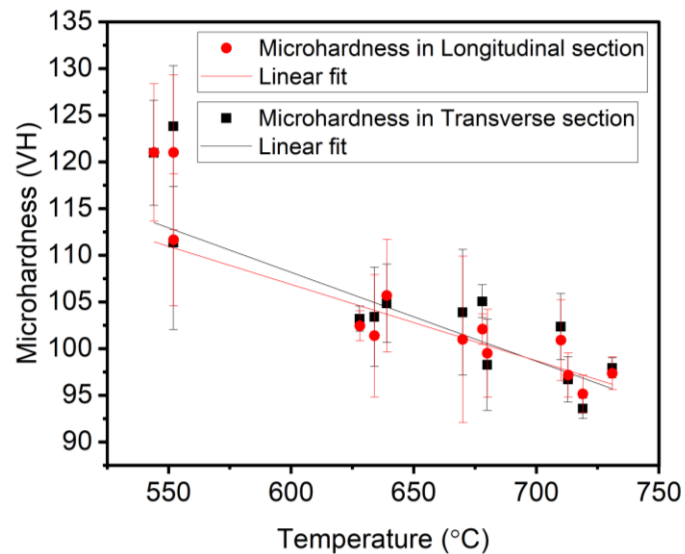


Figure 7: Relation between friction extrusion processing temperature and microhardness obtained for the brass and brass + graphite samples. Lower is the processing temperature, higher is the hardness.

The mechanical performance of the brass rods with and without graphite is further analyzed by conducting tensile tests on selected samples as shown in Figure 8. LFB 7 was selected as the control sample, whereas LFB 9, 13, and 16 were selected as brass/graphite samples based on the hardness values obtained. It is evident from Figure 8 that the brass rod without graphite shows a higher elongation of 45% whereas the brass rods with graphite show average elongation close to 25%. This elongation seen in this study is still higher even though the graphite content is ~7.5% than that reported in the literature (Imai, Kosaka, et al. 2010), where the elongation of brass was reduced below 20% when graphite was added more than 1.25%. Reduced %elongation is typically attributed to the poor wettability of graphite in the Cu-Zn matrix (Imai, Shufeng, et al. 2010). Finally, the average ultimate tensile strength (UTS) of brass/graphite (LFB 16) was seen to be 518 ± 4.1 MPa which is higher than the brass-only control sample LFB 7 with a UTS of 469 ± 8.9 MPa. This improvement in UTS when graphite is added to brass has not been observed in the literature. On the contrary, it has been reported (Imai, Kosaka, et al. 2010) that as the graphite content was increased, the UTS value decreased, which is the opposite of the results from the present study. It is interesting to note that for LFB 9 and 13, the UTS are comparable to the control LFB 7.

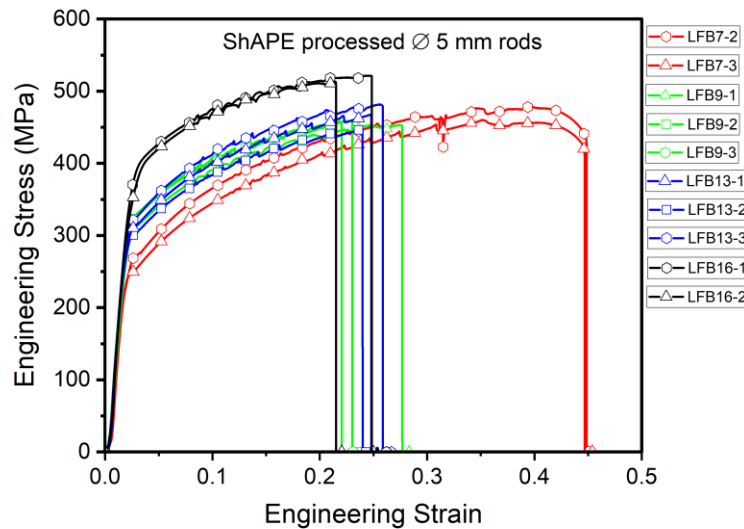


Figure 8: Engineering stress vs strain result of Ø 5 mm friction extrusion processed brass rods

We also compared the mechanical properties of the friction extruded 5 mm diameter rods from the present study with the various brass alloys from Mueller Brass Co. and are presented in Figure 9. For comparison, a few standard brass alloys, lead free Ecostream™ brass alloys, and engineered brass alloys were selected. It is evident from Figure 9 that the UTS of friction extruded brass alloys are on an average higher than the all the other alloys except UNS C67600 which additionally contains tin (Sn) and manganese (Mn). The UTS of friction extruded brass/graphite rod (LFB 16) is comparable to highly leaded UNS C48500 that contains 1.3-2 % Pb. The UNS C67600 also shows highest 0.2% offset yield strength (YS) as shown in Figure 11. In comparison to the other alloys from Mueller, friction extrusion processed samples show excellent yield strength. Although C67600 shows highest UTS and YS, its % elongation is lower than the brass processed in the present study. Therefore, overall, the mechanical properties obtained in the lead free, brass/graphite composites manufactured via friction extrusion provide optimum strength and ductility while being environmentally friendly.

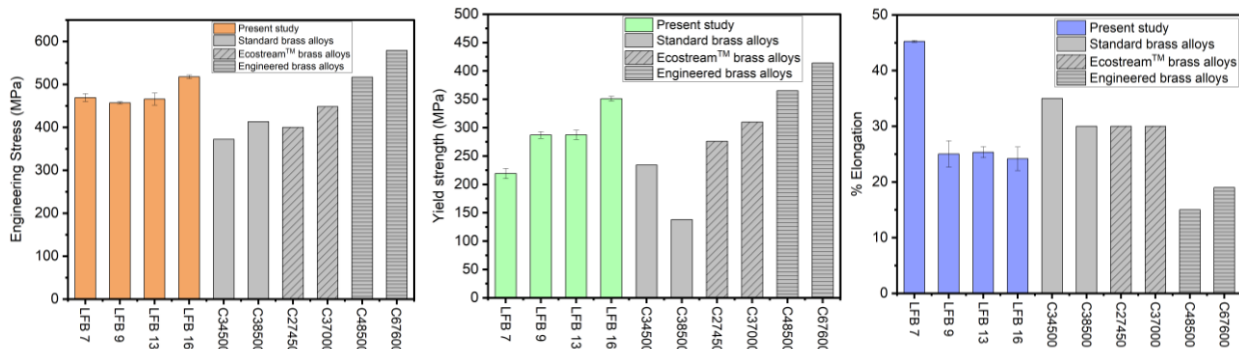


Figure 9: Comparison of ultimate tensile stress (UTS), yield strength (YS), and %elongation in different friction extruded rods with different brass rods from Mueller Brass Co.

Figure 10 presents the hardness and tensile maps of the friction extruded brass and brass-graphite wires with a 2.5 mm diameter. The hardness contour map of the brass-only wire is shown in Figure 10(a). It was observed that the average hardness of the sample at the edge and at the center was $\sim 99 \pm 1$ HV, and $\sim 109 \pm 2$ HV respectively. In contrast, the hardness contour plot of the brass/graphite wire as shown in Figure 10(b) demonstrated a near homogeneous value across the sample. The average hardness of the brass/graphite wire was seen to be $\sim 127 \pm 2$ HV, which is almost 28% higher than that of the average hardness of the brass-only wire. Similar results were observed in the 5 mm diameter rod as well.

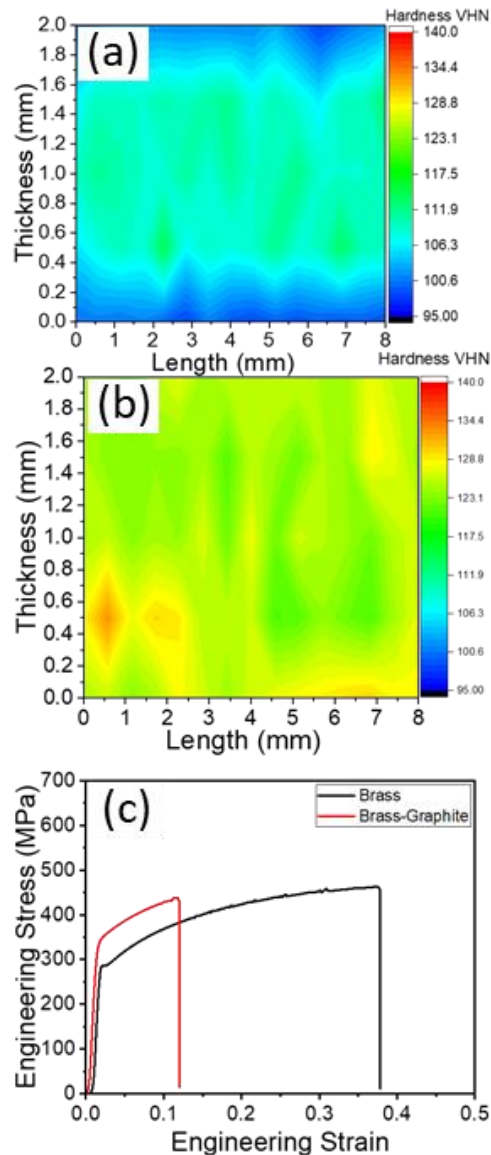


Figure 10: Hardness of (a) brass-only and (b) brass/graphite friction extruded wires; (c). stress-strain behavior of the brass samples manufactured in this project.

The stress-strain behavior of brass-only and brass/graphite is shown in Figure 10(c). A 13% increase in YS was observed in the brass/graphite sample ($\sim 313 \pm 3$ MPa) when compared to that of the brass-only wire ($\sim 278 \pm 2$ MPa). In contrast, the control sample attained a UTS of

$\sim 468 \pm 7$ MPa and %elongation of 40%, when compared to that of the brass + graphite extruded rod with a UTS of $\sim 468 \pm 7$ and %elongation of 11%).

3.3. Microstructural Characterization

The low magnification SEM and high magnification BSED images for brass and brass/graphite powders are shown in the insets of Figure 11. Both the powders appeared faceted and highly irregular in morphology with an average size distribution in the range ~ 70 - $120 \mu\text{m}$. The BSED image brass powders were free from porosity indicating a homogenous mixture of Cu and Zn, as shown in Figure 11 (b1 & b2). In case of brass/graphite powders, the graphite powder showed some amount of agglomeration at various regions which is evident in the EDS showing rich in elemental carbon (C), as seen in Figure 11 (d1-d3).

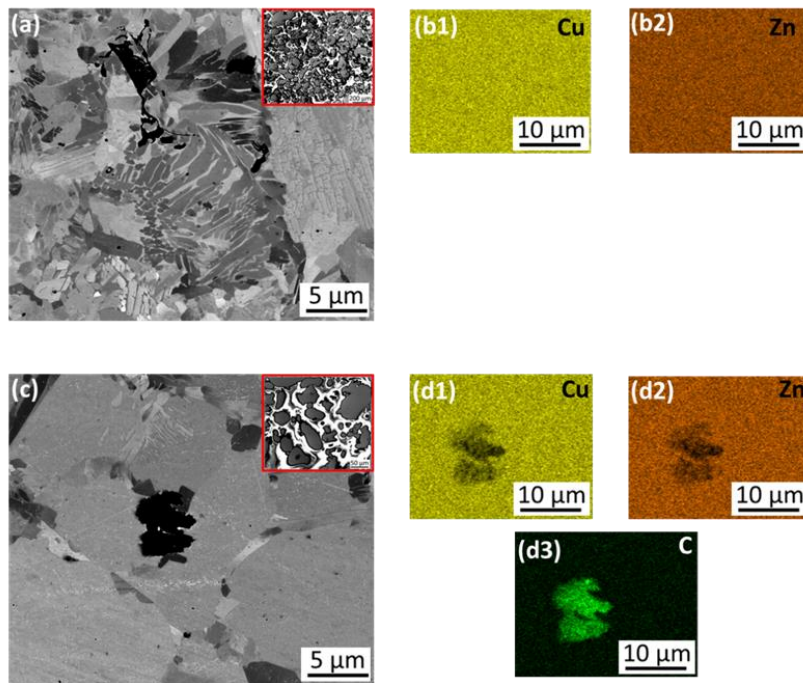


Figure 11: SEM and EDS results of initial: (a)-(b) brass and (c)-(d) brass+graphite powders

Figure 12 shows the microstructure of a representative brass-only ShAPE rod (LFB 7) in longitudinal and transverse sections; similar analyses for other brass-only and brass/graphite ShAPE rods is provided in Appendix C. The microstructures were obtained from several regions to investigate grain size and elemental distributions. Figure 12 (a) shows the location of microstructure from three regions of the longitudinal section and Figure 12 (e) shows the same from the transverse section. The average grain size of LFB 7 sample was about $3.75 \pm 0.38 \mu\text{m}$. A significant grain refinement occurred after friction extrusion due to severe shear deformation of the powders. It is important to note that due to the high processing temperature ($>0.5T_m$), dynamic recrystallization occurs in the rod, which resulted in the formation of equiaxed grains. A bimodal grain size distribution in different regions of the rod as seen in Figure 12(b). The EDS analysis presented in Figure 12 (h) shows the homogenous distribution of Cu and Zn. Since this was the microstructure of a brass-only sample, no C was expected to be present in this case.

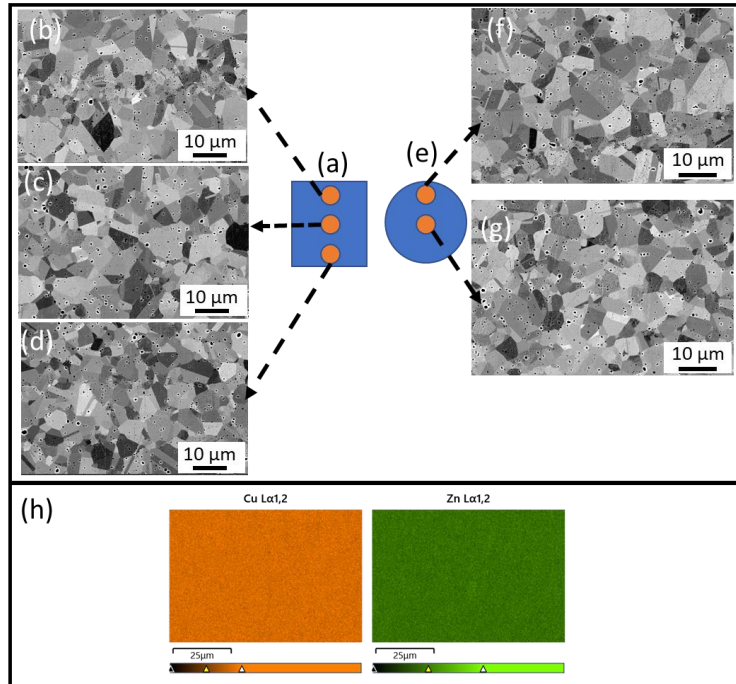


Figure 12: SEM and EDS results of friction extruded $\text{\O} 5\text{mm}$ brass rod LFB 7. (a) and (e) show the schematic of regions on the longitudinal and transverse section respectively for SEM imaging. (b)-(d) SEM microstructure from longitudinal section. (f)-(g) SEM from transverse section. (h) EDS results showing homogenous distribution of Cu and Zn.

Figure 13 illustrates the representative microstructure of a ShAPE brass/graphite rod with a 5-mm-diameter (LFB 16) which demonstrates the highest hardness values. The black regions present were graphite particles confirmed via EDS analysis. The EDS analysis presented also shows a homogenous distribution of Cu and Zn, and C segregations as expected. The equiaxed, circular morphology of graphite in the initial powder (see Figure 11) can be seen to be deformed into an elongated structure at specific locations due to the shear strain applied during processing. Interestingly, the particles appear more equiaxed at the center of the transverse samples. At the edges, the grain size distribution was at a lower size on an average compared to that at the center of the rods. It is understood that the powders experience different amounts of strains during processing. This difference may explain the different morphology of the graphite particles and the grain size in the transverse samples. This observation could explain the variability of hardness in the microstructures in these samples as seen in Section 3.2. It is also curious to see that the graphite particles are aligned in different angles depending on the location as seen in the longitudinal samples. In (b), the particles have an alignment of $\sim 120\text{-}150^\circ$ with respect to the horizontal datum, while in (c), the elongated graphite particles are almost to 0° , and in (d), they are at $\sim 30\text{-}40^\circ$. This alignment of the elongated graphite particles follows an almost 'spiral' deformation pathway which is expected in the ShAPE process, with the pitch being dependent on the local DAPR selected/applied during processing.

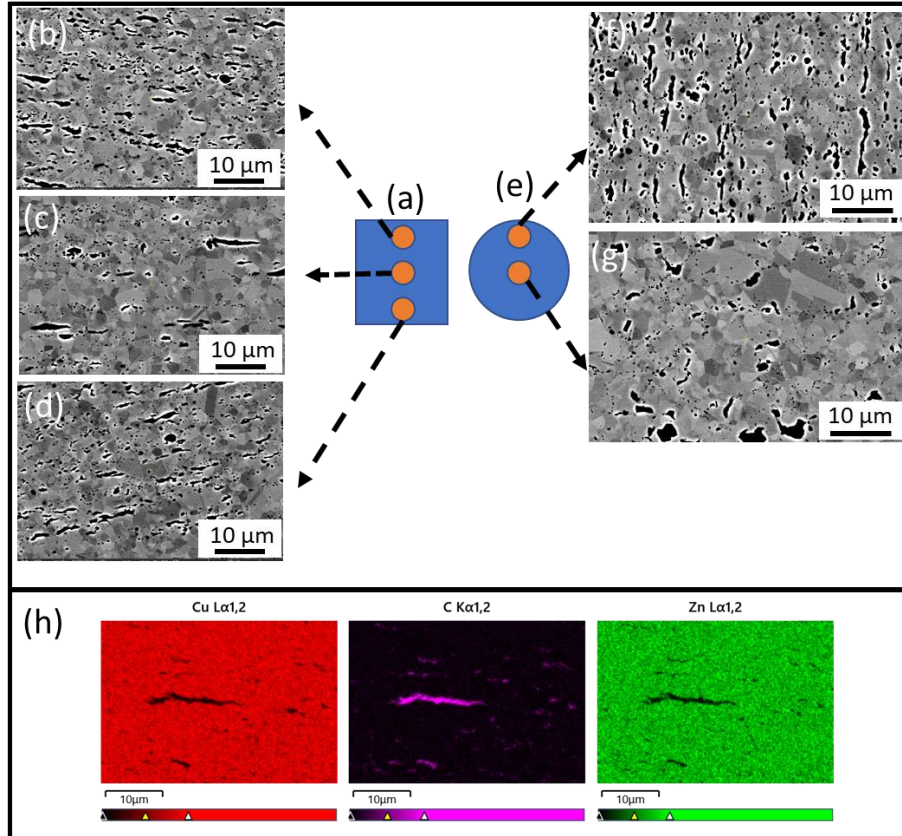


Figure 13: SEM and EDS results of friction extruded $\text{\O} 5\text{mm}$ brass+graphite rod LFB 16. (a) and (e) show the schematic of regions on the longitudinal and transverse section respectively for SEM imaging. (b)-(d) SEM microstructure from longitudinal section. (f)-(g) SEM from transverse section. (h) EDS results showing homogenous distribution of Cu and Zn and presence of carbon sheared during friction extrusion.

Since brass/graphite sample LFB 16 demonstrated the highest hardness, further analysis of its microstructure was performed using EBSD. Samples from transverse sections were selected for the EBSD and the IPF-Z maps along with kernel average misorientation (KAM) maps are shown in Figure 14. The scans were performed closer to the edge and in the center of the rod to reveal the grain size variation. Bimodal grain size distribution were clearly observed. While the grains were relatively smaller near the circumference (EBSD near the edge), they were larger at the center indicating that significant grain growth may have occurred. Grain growth may be attributed to the friction extrusion temperature $>0.5T_m$ which typically results in dynamic recrystallization. Since the surface cools down faster than the center, higher rate of grain growth occurs in the center comparatively leaving the grains near the surface with a smaller size on an average. The KAM maps show the regions of residual stress concentrations in the material after friction extrusion. Note that the regions of stress concentration are present in the smaller grains but not as predominantly in the larger grains indicating that the larger grains are already strain-relieved and recrystallized. Presence of twinned grains could also be observed in the microstructure.

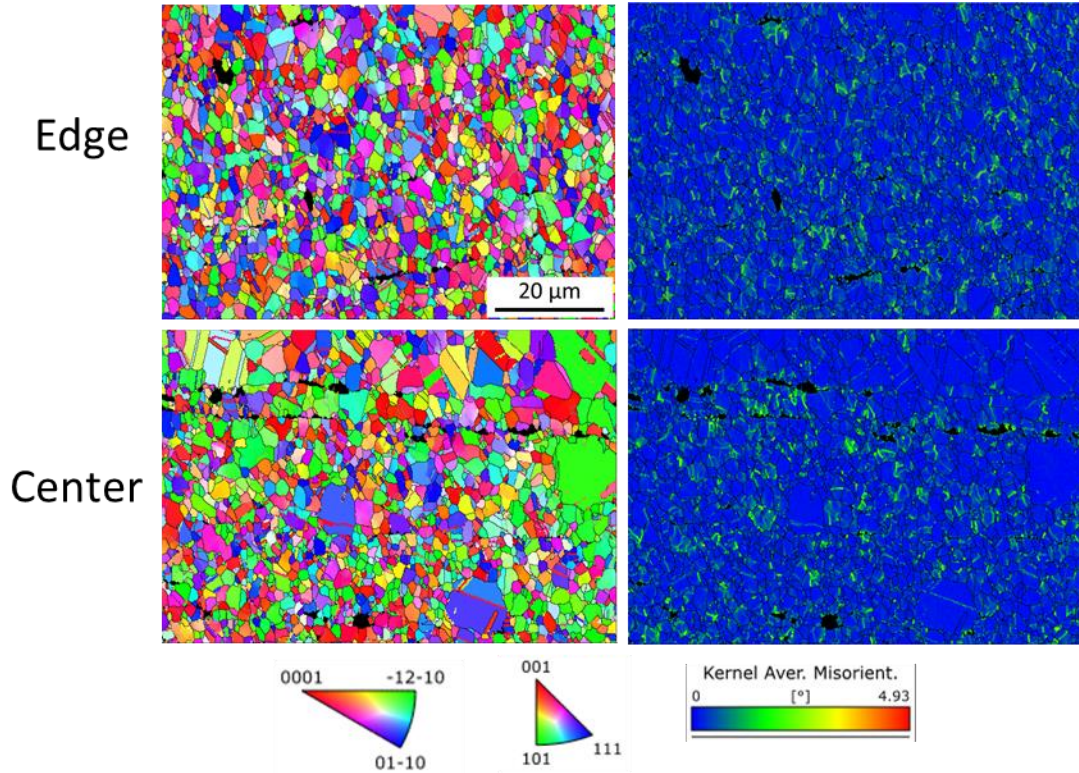


Figure 14: EBSD and KAM images of the brass/graphite friction extruded sample LFB 16 with 5-mm-diameter in the transverse section.

Figure 15 (a) lists the grain size of various 5 mm diameter brass-only and brass/graphite SHAPE rods. It is interesting to note that as the processing temperature decreases, the grain size reduces, which results in higher hardness as per the Hall-Petch relationship (Hansen 2004). Figure 15 (b) and (c) further confirm that the brass samples processed via friction extrusion follow the Hall-Petch relation.

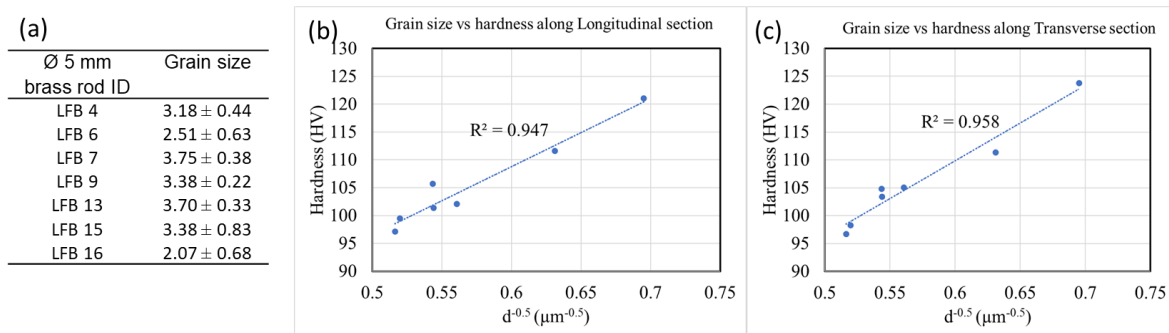


Figure 15: (a) Average grain size of friction extruded Ø 5mm brass and brass+graphite rods. (b) and (c) show the dependence of grain size and hardness along longitudinal and transverse direction of the rods (Hall-Petch relationship)

Figure 16 illustrates the morphologies of graphite particles before and after friction extrusion processing. Considering that the graphite particles are near circular in shape prior to friction extrusion and are stretched to an elongated morphology post processing, with the thickness of the elongated graphite particles being reduced after extrusion.

The extent of deformation for the graphite particles is used to calculate the local strain accumulation according to Dauzenberg and Zaat (Dautzenberg and Zaat 1973):

$$\varepsilon = \left[\frac{D^2/c^2 - 1}{3} \right]^{1/2}$$

where ε is the strain applied on each graphite particle, D is the initial spherical graphite particle size, and c is the thickness of the sheared graphite particle. Based on the reduced thickness of the sheared graphite particles, shear strain induced is when processing the brass/graphite composites is ~122%. At relatively low processing temperatures, the shear-driven forced mixing can be safely assumed to be more dominant, which results in a highly refined microstructure.

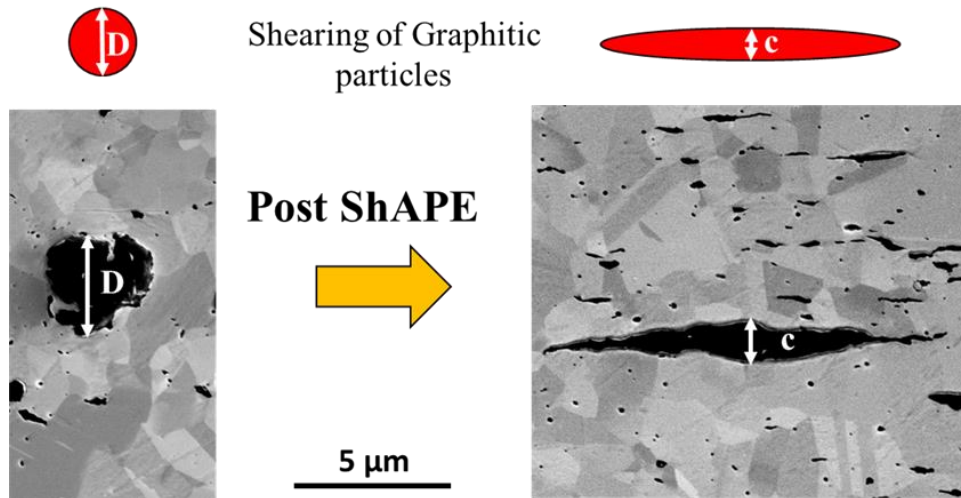


Figure 16: Shearing of graphite particles in brass/graphite composite after friction extrusion.

The transverse and longitudinal microstructures of the start and end positions of the consolidated brass rod section cut for microstructural evaluation were shown in Figure 17. The transverse section of the starting rod showed refined grains all over the sample with a bimodal grain size distribution at the center of the rod, as shown in Figure 17 (a). However, in the case of longitudinal section, as shown in Figure 17 (b), there is no sign of elongated grains in the extrusion direction. In addition, there is a significant grain size variation observed at the center when compared to that of at the edges. The sample attained a weighted average grain size of $\sim 2.9 \pm 0.7 \mu\text{m}$ at the edges and $\sim 1.8 \pm 0.5 \mu\text{m}$ at the center. The decrease in grain size from edge to center can be attributed to a combined effect of variation in temperature and shear deformation from edge to center of the wire. However, in the case of end position of the consolidated extruded rod of the brass sample, as shown in Figure 17 (c and d), the microstructure showed a similar behavior as the starting rod condition, but a relative increase in average grain size distribution. The average grain size was observed to be $\sim 3.2 \pm 0.6 \mu\text{m}$ at the edges and $\sim 2.4 \pm 0.6 \mu\text{m}$ at the center due to the increase in processing temperature (i.e. greater than the recrystallization temperature) at the end of the rod. The average size of the pores was found to be $\sim 0.54 \pm 0.06 \mu\text{m}$ at both the extreme positions of the rod.

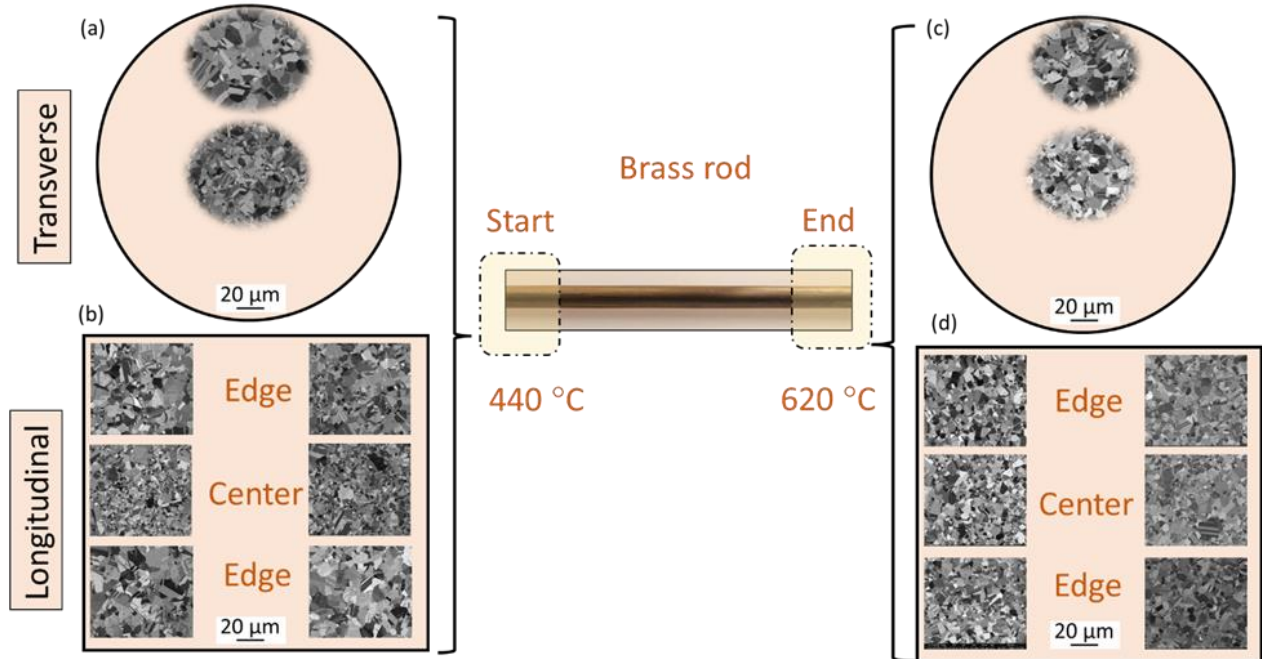


Figure 17: SEM and EDS imaging of the front and end positions of the friction extruded brass-only wire with 2.5 mm diameter in the longitudinal and transverse directions.

The microstructure characterization of the start and end sections of the brass-graphite extrude rod using friction extrusion was shown in **Error! Reference source not found.**. The transverse and the longitudinal sections of the start position for the brass-graphite rod microstructures were shown in (a) and (b). The microstructure in the transverse and longitudinal sections reveal that the grains are refined with a bimodal grain size distribution throughout the samples. In addition, the graphite showed a near circular morphology in the transverse section at both the edge and center, whereas in the longitudinal sections, the graphite showed an elongated shear irregular plate like structure. It is also interesting to notice that the grain refinement is severe and evident near the regions where the graphite is sheared.

Based on the microstructure evolution, the average grain size was calculated to be $\sim 1.8 \pm 0.2 \mu\text{m}$ at the edges and $\sim 1.0 \pm 0.7 \mu\text{m}$ at the center. Similar microstructure behavior was observed for the transverse and longitudinal sections of the end position of the rod. In case of the end section, the microstructure showed a similar graphite morphology as the longitudinal section, as shown in (c) and (d). The EDS elemental map distribution shows the uniform distribution of Cu and Zn in the matrix, and rich in elemental C in the dark spots and patches, indicating the presence of graphite in the extruded rods. Almost similar grain size distribution was attained at the edge ($\sim 1.2 \pm 0.6 \mu\text{m}$) and center ($\sim 0.9 \pm 0.3 \mu\text{m}$) of the sections when compared to that of the starting brass-graphite rod. The overall grain size of the brass-graphite sample showed a two-fold decrease in grain size when compared to controlled extruded rod, which could be due to the presence of a strong graphite phase.

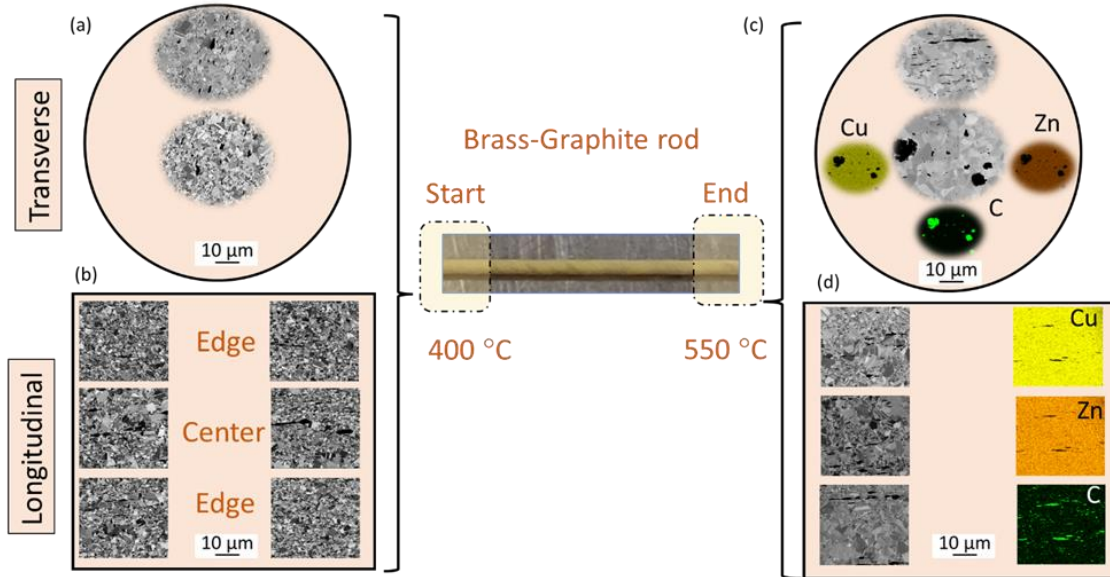


Figure 18. SEM and EDS imaging of the front and end positions of the friction extruded brass/graphite wire with 2.5 mm diameter in the longitudinal and transverse directions.

The EBSD results for the 2.5 mm diameter brass/graphite friction extruded rod is shown in Figure 19. Images were obtained from the center and from near the edge of the rod. The black elongation regions in the edge region of EBSD scan are graphite whereas it is not present in the center image. Since graphite is distributed sporadically, it was not captured in the localized region that was observed for EBSD. SEM images at lower magnification show the distribution of graphite. Similar to the 5 mm diameter rod, in the 2.5 mm diameter rod as well the grains are larger in the center and smaller near the edges due to the difference in recrystallization, grain growth, and faster cooling rate at the edges. The KAM maps show the region of higher stress concentration in the smaller grains, whereas the larger grains are already stress relieved after recrystallization. Presence of twinned grains similar to Figure 14 could also be observed in this case.

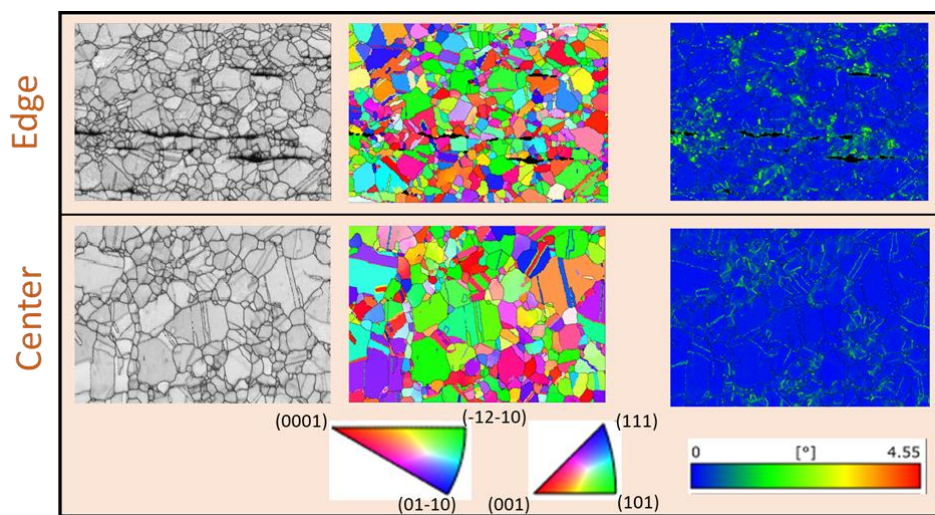


Figure 19: EBSD and KAM imaging of friction extruded 2.5 mm brass/graphite wire in the transverse direction at the center and edge of the wire.

Figure 20 further reveals the microstructure and compositional evolution at the atomic scale of the 2.5 mm wire brass/graphite wire using TEM analysis. Figure 20 (a) shows the area where the FIB (Focused Ion Beam) lift out was performed for further TEM investigation that included both the matrix and the graphite region, as seen in the inset.

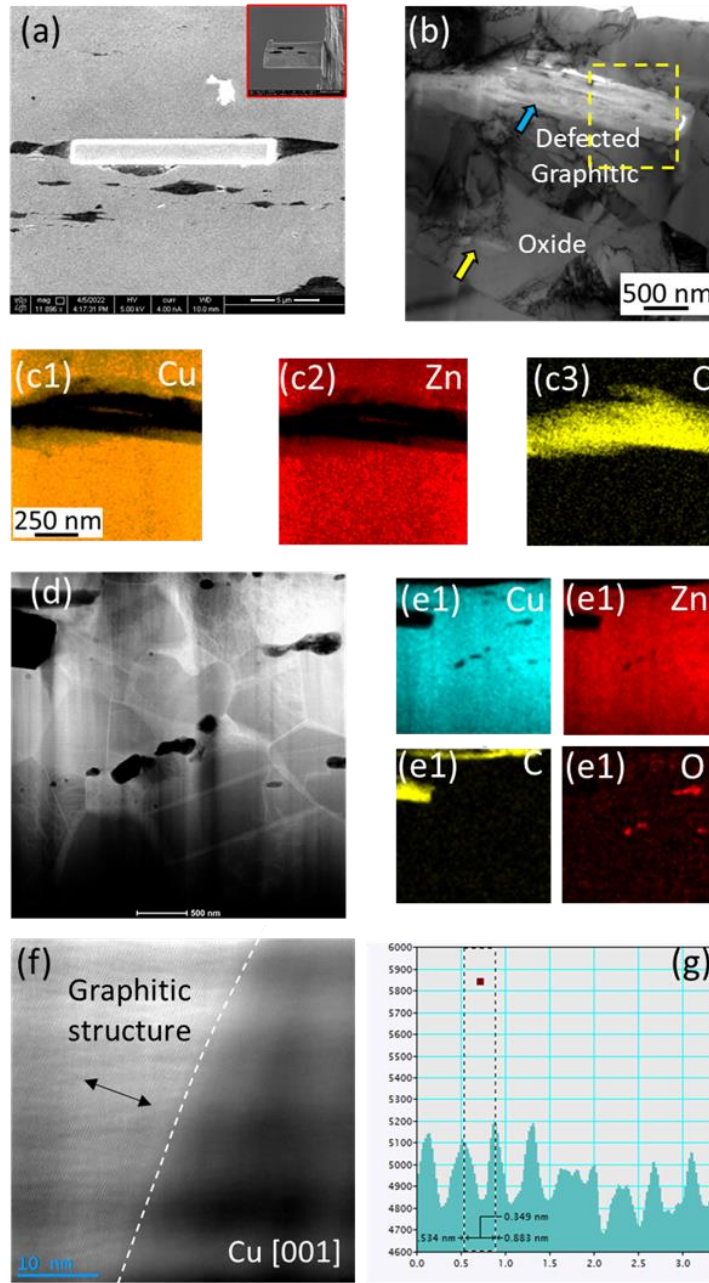


Figure 20: TEM results of friction extruded 2.5 mm diameter brass/graphite wire. (a) Area from where FIB lift out was performed. (b) Bright field TEM (c) EDS of the sheared graphite region. (d) STEM image (e) STEM-EDS maps (f) Transition in the [001] zone axis of the Cu and graphite. (g)

The bright field TEM (BFTEM) image in Figure 20 (b) shows the sheared defected graphite particles indicated by the cyan arrow and the formation of discontinuous oxide particles formed during consolidation, as indicated by the yellow arrow. The EDS elemental map of the sheared

graphite region, as seen in Figure 20 (c1-c3), shows co-shearing of graphite and brass, indicating the large shear strain of the secondary particles into the matrix. Apart from defected graphite, there were other fragmented phases that were revealed using STEM image, as shown in Figure 20 (d). As illustrated by the STEM-EDS maps in Figure 20 (e1-e4), there were nanoscale oxides (rich in zinc and oxygen), embedded in the matrix that established the next level of the microstructural hierarchy. The phase contrast image in Figure 20 (f) shows a clear transition in the [001] zone axis of the Cu grain and graphitic structure. In addition, the inter d-spacing profile of the graphitic structure is 0.349 which is equivalent of (002) plane of the graphite.

4. Conclusions

In this project, one step synthesis techniques were developed to manufacture lead free brass-only and brass/graphite wires, rods and tubes using solid phase processing techniques, namely friction extrusion and ShAPE. The lead-free brass feedstock powders with an average size of ~70 – 120 μm were supplied by Mueller International. Wires with a diameter of 2.5 mm and rods of diameter of 5 mm were developed; additionally, pathway for manufacturing tubes with 12 mm OD and 1 mm wall thickness were also demonstrated. Friction extrusion and ShAPE tooling was developed in this project to enable the synthesis of the lead-free brass composites. Different tool feed rate and rotation rate combinations were explored to identify the evolution of material flow and process temperatures during extrusion, and their effects on the formation of consolidated wires, rods, and tubes with minimal surface defects.

Hardness measurements of 5-mm-diameter brass-only and brass/graphite friction extruded rods showed a dependence of the property on processing conditions. At lower temperatures and high feed rate, hardness values as high as 123 Hv were observed for the brass/graphite rods. A variation in the cross-sections of the rods was observed with higher values registered towards the edges of the samples. Tensile testing showed that the ultimate tensile strength of the brass/graphite rods was 10% higher than that of brass-only friction extruded rods. Literature review showed that the UTS of friction extruded brass/graphite alloys was higher in general compared to lead free Ecostream™ brass alloys except UNS C67600 which additionally contains tin (Sn) and manganese (Mn). Hardness values across the 2.5 mm diameter brass/graphite wires was more uniform in general; these samples also showed ~127 Hv which was about 28% higher than the corresponding control wires manufactured without the graphite additives.

Scanning electron microscopy of brass-only and brass/graphite rods and wires showed a bimodal grain size distribution in general with larger grains occurring at the center of the rods and smaller ones seen towards the center. In both the rods and wires, the average grain size in brass-only rods was about twice of that seen in the brass/graphite rods, possibly due to the grain refinement brought about by the graphite inclusions. Energy dispersive analysis confirmed uniform distributions of copper and zinc in all the friction extruded samples, while the brass/graphite rods and wires showed streaks of elongated carbon species that were concluded to be strained graphite particles. In the feedstock powder imaging, it was seen that the graphite particles were more equiaxed in nature. Electron backscatter diffraction showed that the grains in both the brass-only and brass/graphite composites were equiaxed. Kernel average misorientation maps showed higher density of deformation in the smaller grains plausibly due to the larger grains formed after recrystallization since the extrusion temperatures were in general higher than half that of the brass melting temperatures. Based on the reduced thickness of the sheared graphite particles, shear strain induced during processing the brass/graphite composite rods during friction extrusion was estimated to be ~122%. Transmission electron microscopy of the brass/graphite wire samples showed co-shearing of graphite and brass, along with nanoscale oxides (rich in zinc and oxygen), embedded in the matrix.

This study presents the first ever proof-of-concept demonstration of a one-step approach to manufacturing lead free brass/graphite composites with mechanical performance similar to commercial equivalents. Further developmental activities demonstrating larger component form factors, as well as evaluating the effects of post-processing them are essential in assessing the commercialization potential of friction extruded and ShAPE-synthesized lead free brass composites.

References

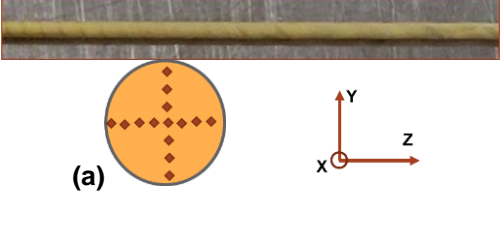
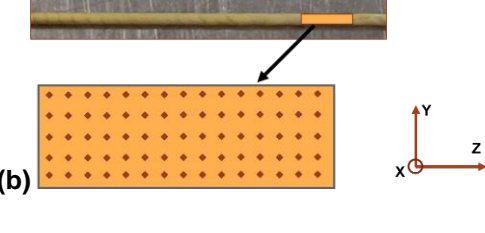
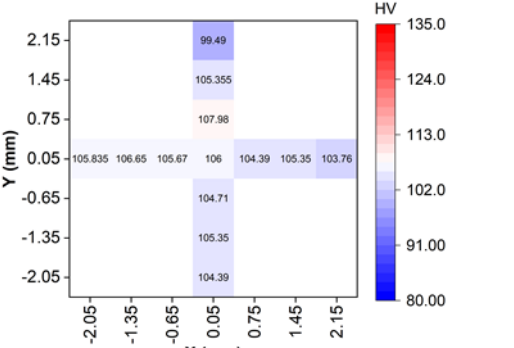
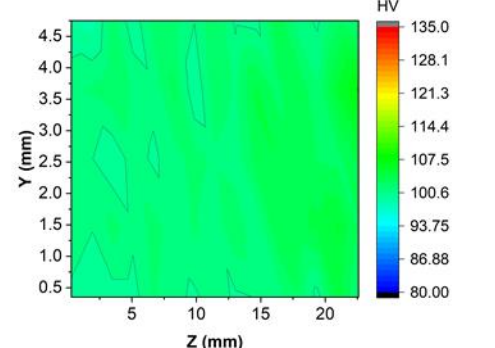
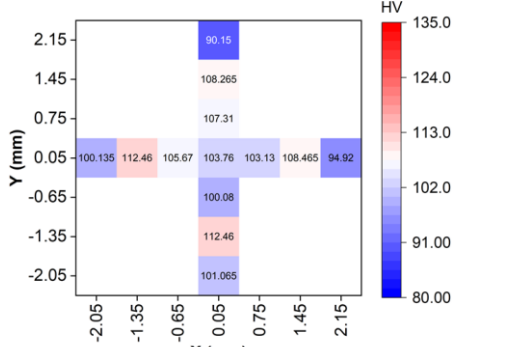
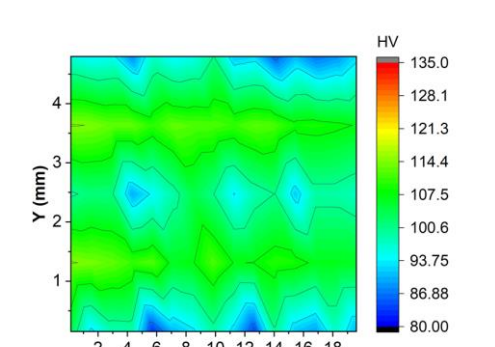
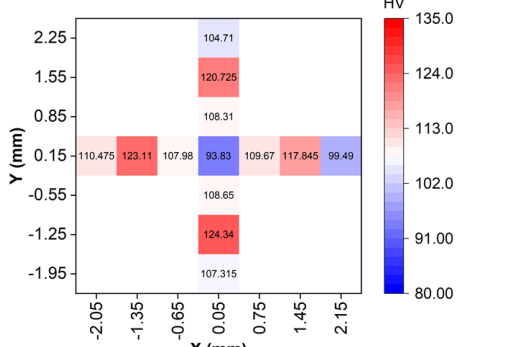
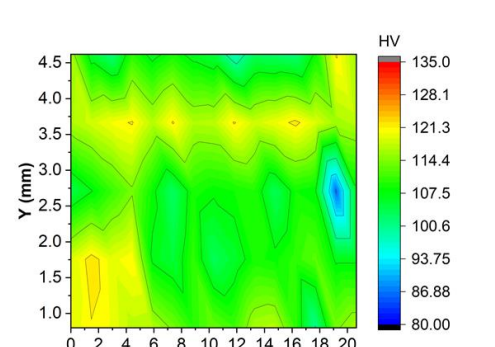
- Dautzenberg, JH, and JH Zaat. 1973. "Quantitative determination of deformation by sliding wear." *Wear* 23 (1):9-19.
- Ghorbani, M., M. Mazaheri, K. Khangholi, and Y. Kharazi. 2001. "Electro deposition of graphite-brass composite coatings and characterization of the tribological properties." *Surface & Coatings Technology* 148 (1):71-76.
- Hansen, Niels. 2004. "Hall–Petch relation and boundary strengthening." *Scripta materialia* 51 (8):801-806.
- Imai, Hisashi, Yoshiharu Kosaka, Akimichi Kojima, Shufeng Li, Katsuyoshi Kondoh, Junko Umeda, and Haruhiko Atsumi. 2010. "Characteristics and machinability of lead-free P/M Cu60–Zn40 brass alloys dispersed with graphite." *Powder Technology* 198 (3):417-421. doi: <https://doi.org/10.1016/j.powtec.2009.12.010>.
- Imai, Hisashi, Li Shufeng, Haruhiko Atsumi, Yoshiharu Kosaka, Akimichi Kojima, and Katsuyoshi Kondoh. 2010. "Development of lead-free machinable brass with bismuth and graphite particles by powder metallurgy process." *Materials transactions* 51 (5):855-859.
- Li, S., H. Imai, J. Umeda, Y. Fu, and K. Kondoh. 2016. "Investigation of High-strength Lead-free Machinable Cu40Zn Duplex Graphite Brasses by Powder Metallurgy." *Materials Science and Technology* 32 (17):1751-1756.
- Stoddart, C. T. H., C. Lea, W. A. Dench, P. Green, and H. R. Pettit. 1979. "Relationship between lead content of Cu–40Zn, machinability, and surface composition determined by Auger electron spectroscopy." *Metals Technology* 6 (1):176-184. doi: 10.1179/030716979803276435.
- Whalen, Scott A., Keerti S. Kappagantula, MD Reza E Rabby, Xiao Li, Nicole R. Overman, Matthew J. Olszta, Tianhao Wang, Darrell R. Herling, Sarah R. Suffield, Timothy J. Roosendaal, Brandon S. Taysom, Julian D. Escobar Atehortua, Joshua A. Silverstein, Nathan L. Canfield, and Daniel D. Graff. 2021. Shear Assisted Processing and Extrusion (ShAPE) of Aluminum Alloy 7075, 2024, and Al-12.4TM. United States.
- Zhang, X., C. Ma, S. F. Li, D. Pan, and F. Y. Zheng. 2020. "Interface design of lead-free free-cutting titanium reinforced graphite brass composites and its effect on mechanical properties and cutting performance." *Materials Science and Engineering a-Structural Materials Properties Microstructure and Processing* 774.

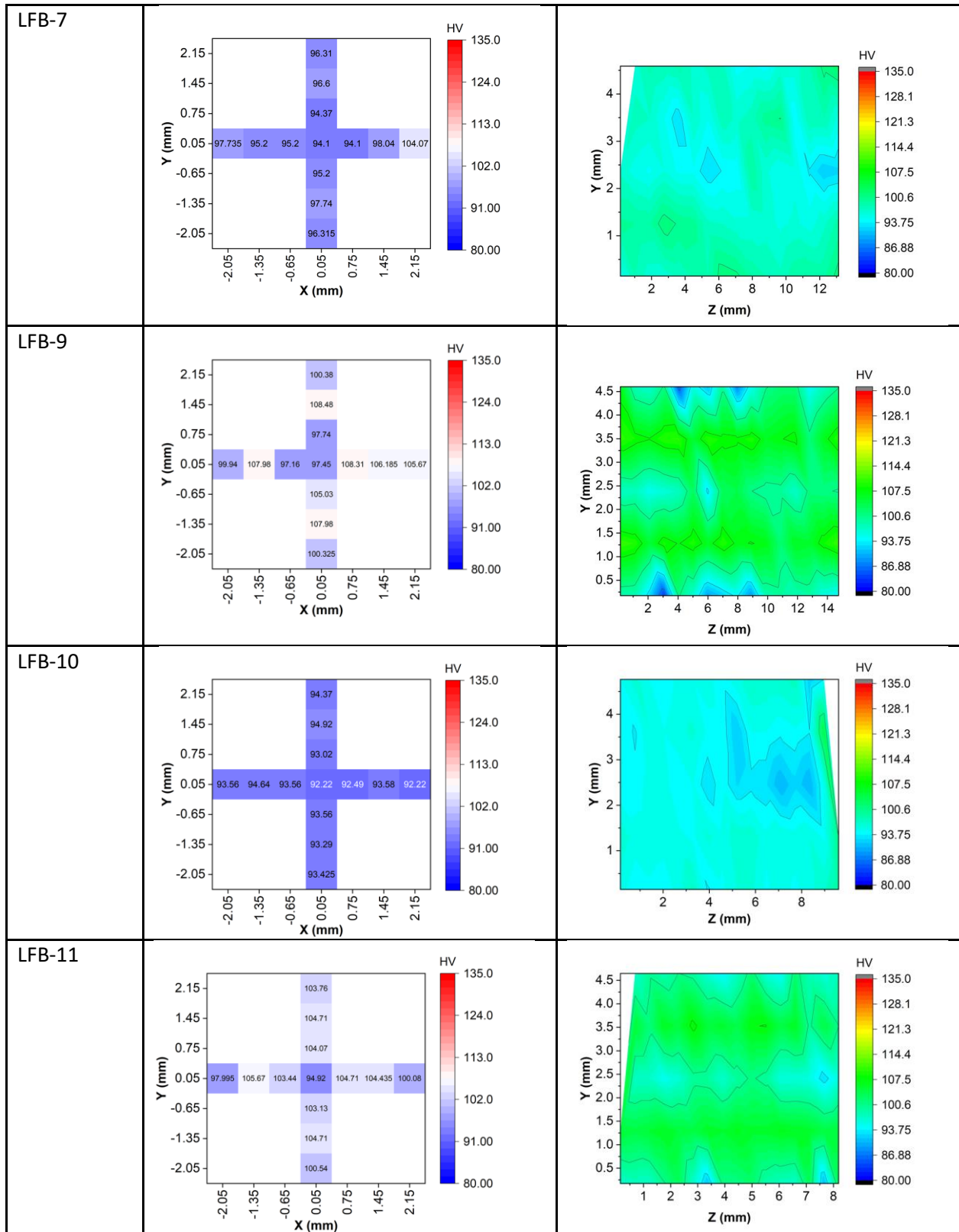
Appendix A – ShAPE Process Parameters for Manufacturing Lead Free Brass Components

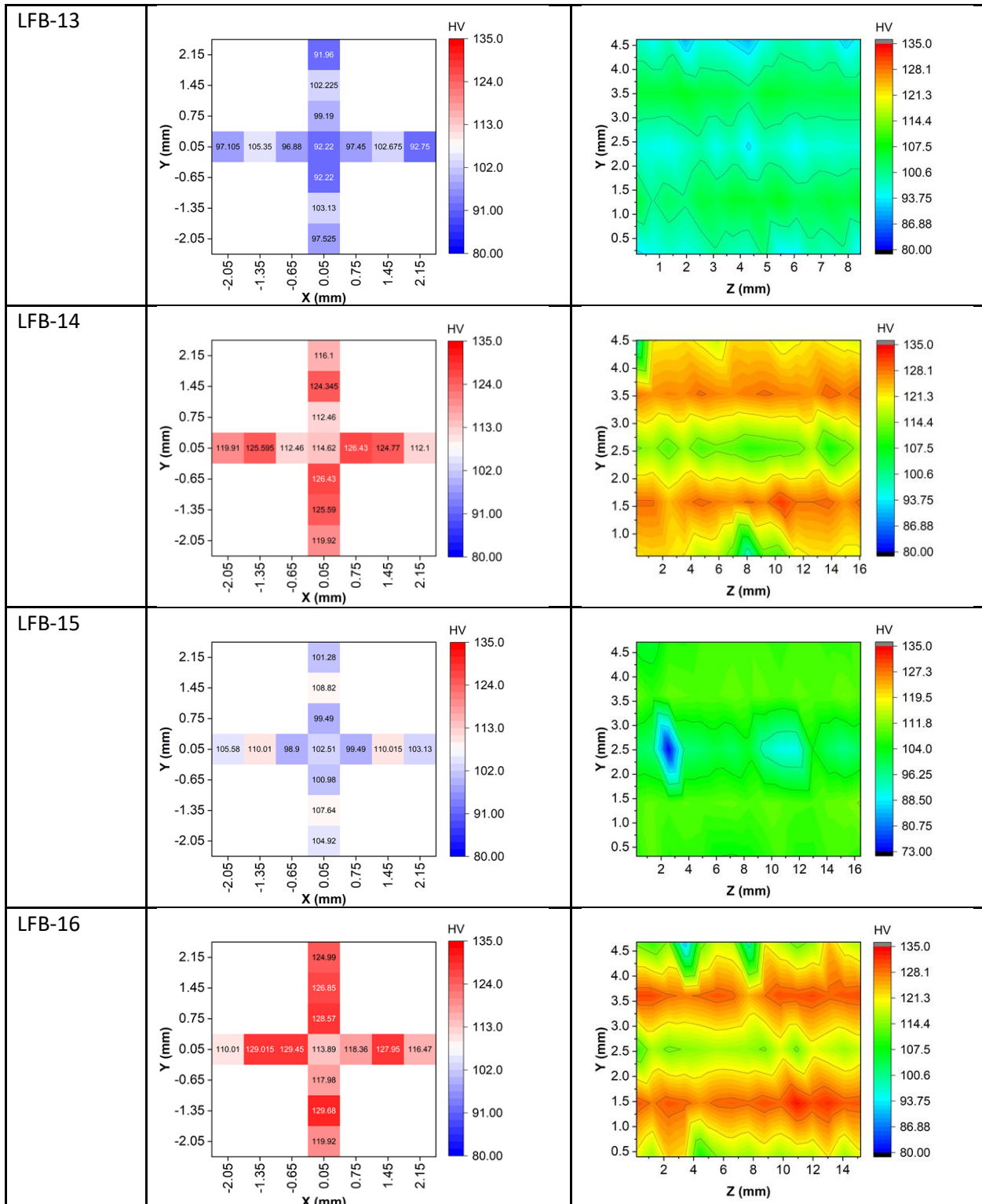
Table 2. Trials and corresponding control parameters and response variables during friction extrusions and ShAPE process

Trial #	Precursor Material	Rotation Rate Adjusted	Steady Feed Rate	Temperature Beginning-end	Avg. End Force	Wire Length
		RPM	mm/min	°C	kN	mm
LFB 1	LFB (Control)	50-30	4	500-620	200	760
LFB 2	LFB+Graphite	50	4	540-560	240	890
LFB 3	LFB (Control)	50-40	4	530-660	45	475
LFB 4	LFB (Control)	50	16	500-700	90	370
LFB 5	LFB+Graphite	50	16	600-660	90	530
LFB 6	LFB+Graphite	60-83	24	435-560	110	495
LFB 7	LFB (Control)	100-60	8	450-730	45	470
LFB 8	LFB+Graphite	100-150	8	360-550	45	570
LFB 9	LFB+Graphite	100-240	8	450-650	25	565
LFB 10	LFB (Control)	450-60	8	500-730	37	485
LFB 11	LFB+Graphite	450-220	8	500-740	25	540
LFB 12	LFB+Graphite	450-400	24	-	27	520
LFB 13	LFB+Graphite	450-300	24	600-720	30	540
LFB 14	LFB+Graphite	100-150	4	470-570	60	
LFB 15	LFB+Graphite	100-350	4	570-640	30	
LFB 16	LFB+Graphite	200-100	4	420-570	54	
LFB 17	LFB (Control)	150-40	4	500-640	54	350
LFB 18	LFB+Graphite	250-200	4	500-560	64	450
LFB 19	LFB (Control)	210-80	24	-	34	380
LFB 20	LFB (Control)	240-100	24	500-740	64	400
LFB 21	LFB+Graphite	200-60	24	500-650	120	455
LFB 22	LFB+Graphite	150-70	4	500-550	70	520
LFB 23	LFB+Graphite	150-70	4	500-550	75	525
LFB 24	LFB+Graphite	150-105	4	500-550	75	750
LFB 25	LFB+Graphite	170-70	4	500-550	90	550
LFB 26	LFB+Graphite	150-80	24	680-600	150	570
LFB 27	LFB+Graphite	150-75	24	550-600	140	580

Appendix B – Mechanical Properties and Microstructural Images of Lead-Free Brass Components Manufactured via ShAPE

Sample ID	Microhardness in Transverse section	Microhardness in Longitudinal section																																																																
	 <p>(a)</p>	 <p>(b)</p>																																																																
LFB-4	 <table border="1"> <caption>Microhardness Data for LFB-4 (Transverse)</caption> <thead> <tr> <th>Y (mm)</th> <th>X = -2.05</th> <th>X = -1.35</th> <th>X = -0.65</th> <th>X = 0.05</th> <th>X = 0.75</th> <th>X = 1.45</th> <th>X = 2.15</th> </tr> </thead> <tbody> <tr> <td>2.15</td> <td></td> <td></td> <td></td> <td>99.49</td> <td></td> <td></td> <td></td> </tr> <tr> <td>1.45</td> <td></td> <td></td> <td></td> <td>105.355</td> <td></td> <td></td> <td></td> </tr> <tr> <td>0.75</td> <td></td> <td></td> <td></td> <td>107.98</td> <td></td> <td></td> <td></td> </tr> <tr> <td>0.05</td> <td>105.835</td> <td>106.65</td> <td>105.67</td> <td>106</td> <td>104.39</td> <td>105.35</td> <td>103.76</td> </tr> <tr> <td>-0.65</td> <td></td> <td></td> <td></td> <td>104.71</td> <td></td> <td></td> <td></td> </tr> <tr> <td>-1.35</td> <td></td> <td></td> <td></td> <td>105.35</td> <td></td> <td></td> <td></td> </tr> <tr> <td>-2.05</td> <td></td> <td></td> <td></td> <td>104.39</td> <td></td> <td></td> <td></td> </tr> </tbody> </table>	Y (mm)	X = -2.05	X = -1.35	X = -0.65	X = 0.05	X = 0.75	X = 1.45	X = 2.15	2.15				99.49				1.45				105.355				0.75				107.98				0.05	105.835	106.65	105.67	106	104.39	105.35	103.76	-0.65				104.71				-1.35				105.35				-2.05				104.39				
Y (mm)	X = -2.05	X = -1.35	X = -0.65	X = 0.05	X = 0.75	X = 1.45	X = 2.15																																																											
2.15				99.49																																																														
1.45				105.355																																																														
0.75				107.98																																																														
0.05	105.835	106.65	105.67	106	104.39	105.35	103.76																																																											
-0.65				104.71																																																														
-1.35				105.35																																																														
-2.05				104.39																																																														
LFB-5	 <table border="1"> <caption>Microhardness Data for LFB-5 (Transverse)</caption> <thead> <tr> <th>Y (mm)</th> <th>X = -2.05</th> <th>X = -1.35</th> <th>X = -0.65</th> <th>X = 0.05</th> <th>X = 0.75</th> <th>X = 1.45</th> <th>X = 2.15</th> </tr> </thead> <tbody> <tr> <td>2.15</td> <td></td> <td></td> <td></td> <td>90.15</td> <td></td> <td></td> <td></td> </tr> <tr> <td>1.45</td> <td></td> <td></td> <td></td> <td>108.265</td> <td></td> <td></td> <td></td> </tr> <tr> <td>0.75</td> <td></td> <td></td> <td></td> <td>107.31</td> <td></td> <td></td> <td></td> </tr> <tr> <td>0.05</td> <td>100.135</td> <td>112.46</td> <td>105.67</td> <td>103.76</td> <td>103.13</td> <td>108.465</td> <td>94.92</td> </tr> <tr> <td>-0.65</td> <td></td> <td></td> <td></td> <td>100.08</td> <td></td> <td></td> <td></td> </tr> <tr> <td>-1.35</td> <td></td> <td></td> <td></td> <td>112.46</td> <td></td> <td></td> <td></td> </tr> <tr> <td>-2.05</td> <td></td> <td></td> <td></td> <td>101.065</td> <td></td> <td></td> <td></td> </tr> </tbody> </table>	Y (mm)	X = -2.05	X = -1.35	X = -0.65	X = 0.05	X = 0.75	X = 1.45	X = 2.15	2.15				90.15				1.45				108.265				0.75				107.31				0.05	100.135	112.46	105.67	103.76	103.13	108.465	94.92	-0.65				100.08				-1.35				112.46				-2.05				101.065				
Y (mm)	X = -2.05	X = -1.35	X = -0.65	X = 0.05	X = 0.75	X = 1.45	X = 2.15																																																											
2.15				90.15																																																														
1.45				108.265																																																														
0.75				107.31																																																														
0.05	100.135	112.46	105.67	103.76	103.13	108.465	94.92																																																											
-0.65				100.08																																																														
-1.35				112.46																																																														
-2.05				101.065																																																														
LFB-6	 <table border="1"> <caption>Microhardness Data for LFB-6 (Transverse)</caption> <thead> <tr> <th>Y (mm)</th> <th>X = -2.05</th> <th>X = -1.35</th> <th>X = -0.65</th> <th>X = 0.05</th> <th>X = 0.75</th> <th>X = 1.45</th> <th>X = 2.15</th> </tr> </thead> <tbody> <tr> <td>2.25</td> <td></td> <td></td> <td></td> <td>104.71</td> <td></td> <td></td> <td></td> </tr> <tr> <td>1.55</td> <td></td> <td></td> <td></td> <td>120.725</td> <td></td> <td></td> <td></td> </tr> <tr> <td>0.85</td> <td></td> <td></td> <td></td> <td>108.31</td> <td></td> <td></td> <td></td> </tr> <tr> <td>0.15</td> <td>110.475</td> <td>123.11</td> <td>107.98</td> <td>93.83</td> <td>109.67</td> <td>117.845</td> <td>99.49</td> </tr> <tr> <td>-0.55</td> <td></td> <td></td> <td></td> <td>108.65</td> <td></td> <td></td> <td></td> </tr> <tr> <td>-1.25</td> <td></td> <td></td> <td></td> <td>124.34</td> <td></td> <td></td> <td></td> </tr> <tr> <td>-1.95</td> <td></td> <td></td> <td></td> <td>107.315</td> <td></td> <td></td> <td></td> </tr> </tbody> </table>	Y (mm)	X = -2.05	X = -1.35	X = -0.65	X = 0.05	X = 0.75	X = 1.45	X = 2.15	2.25				104.71				1.55				120.725				0.85				108.31				0.15	110.475	123.11	107.98	93.83	109.67	117.845	99.49	-0.55				108.65				-1.25				124.34				-1.95				107.315				
Y (mm)	X = -2.05	X = -1.35	X = -0.65	X = 0.05	X = 0.75	X = 1.45	X = 2.15																																																											
2.25				104.71																																																														
1.55				120.725																																																														
0.85				108.31																																																														
0.15	110.475	123.11	107.98	93.83	109.67	117.845	99.49																																																											
-0.55				108.65																																																														
-1.25				124.34																																																														
-1.95				107.315																																																														





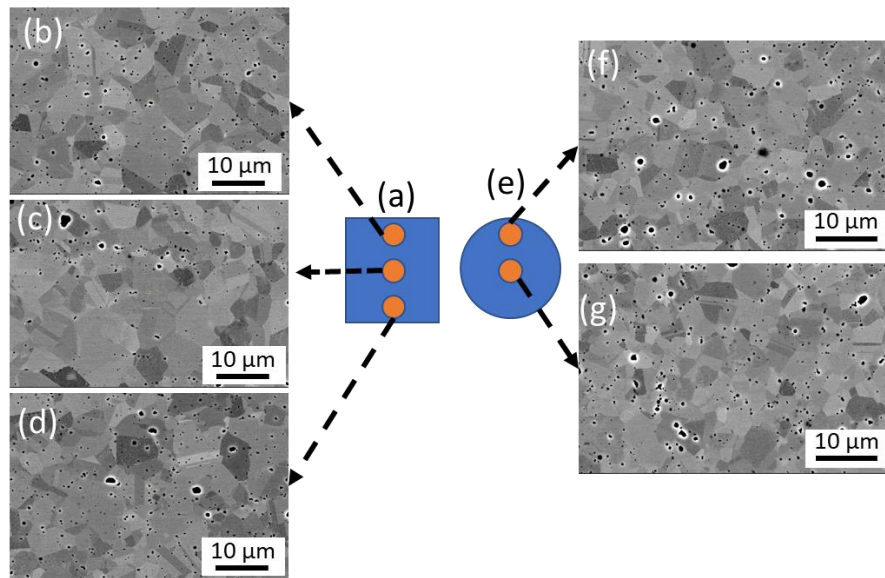
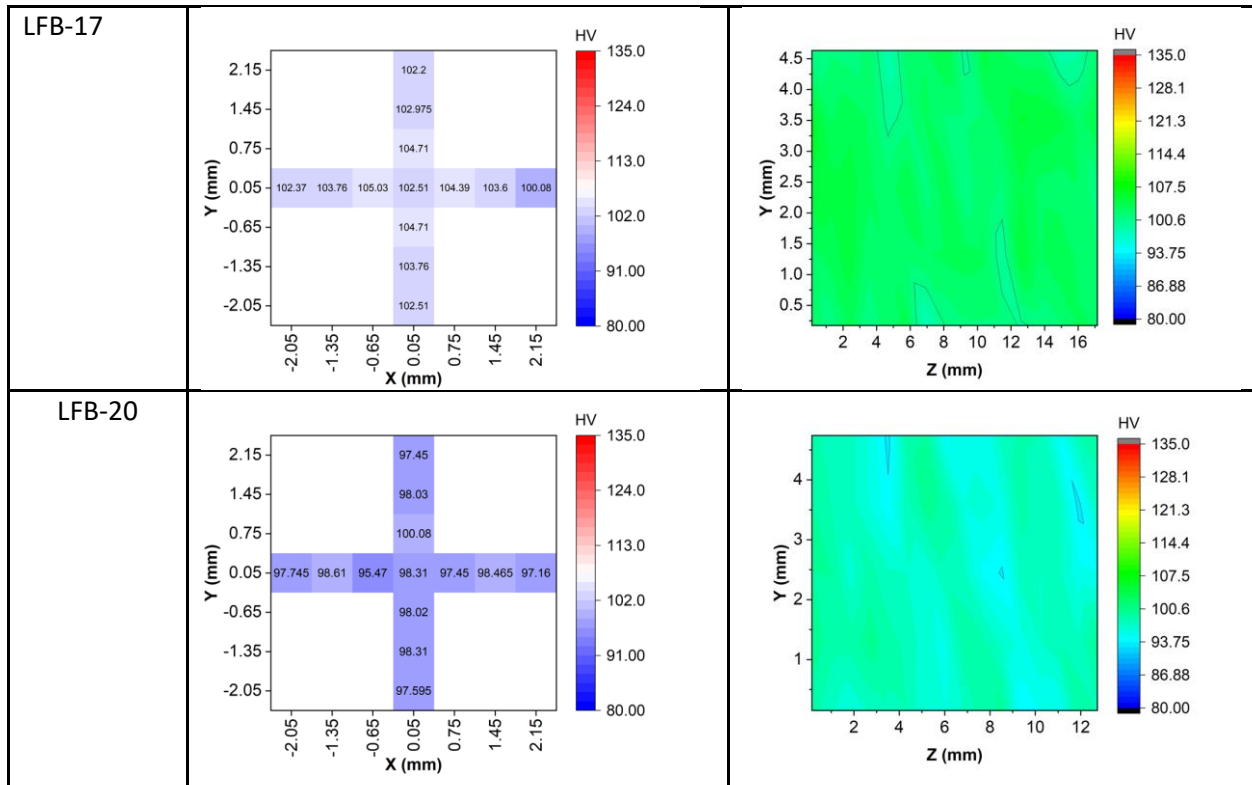


Figure 21 SEM and EDS results of friction extruded $\text{\O} 5\text{mm}$ brass rod LFB 4. (a) and (e) show the schematic of regions on the longitudinal and transverse section respectively for SEM imaging. (b)-(d) SEM microstructure from longitudinal section. (f)-(g) SEM from transverse section.

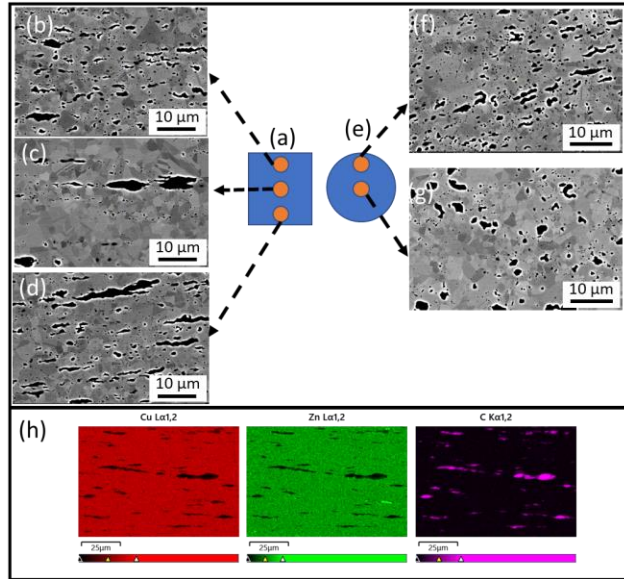


Figure 22. SEM and EDS results of friction extruded \varnothing 5mm brass + graphite rod LFB 6. (a) and (e) show the schematic of regions on the longitudinal and transverse section respectively for SEM imaging. (b)-(d) SEM microstructure from longitudinal section. (f)-(g) SEM from transverse section. (h) EDS results showing homogenous distribution of Cu and Zn and presence of carbon sheared during friction extrusion.

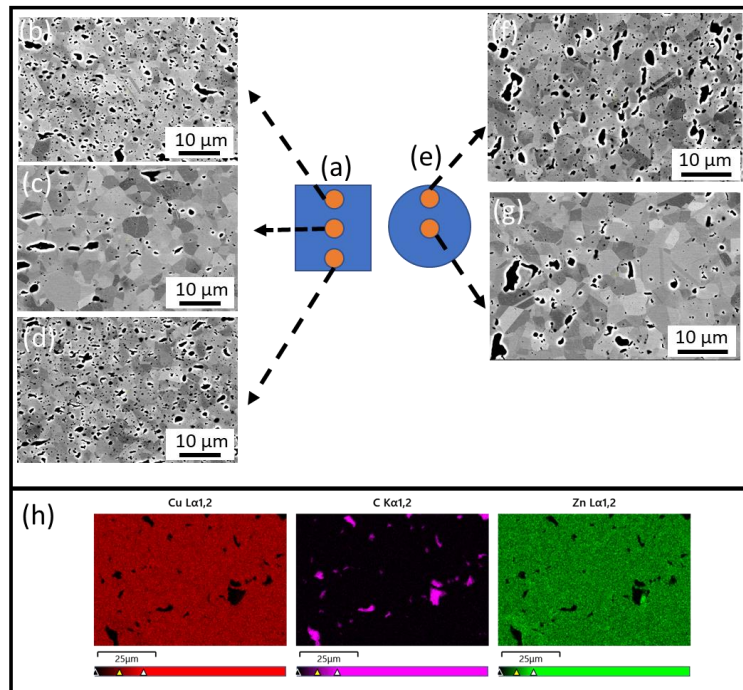


Figure 23. SEM and EDS results of friction extruded \varnothing 5mm brass + graphite rod LFB 15. (a) and (e) show the schematic of regions on the longitudinal and transverse section respectively for SEM imaging. (b)-(d) SEM microstructure from longitudinal section. (f)-(g) SEM from transverse section. (h) EDS results showing homogenous distribution of Cu and Zn and presence of carbon sheared during friction extrusion.

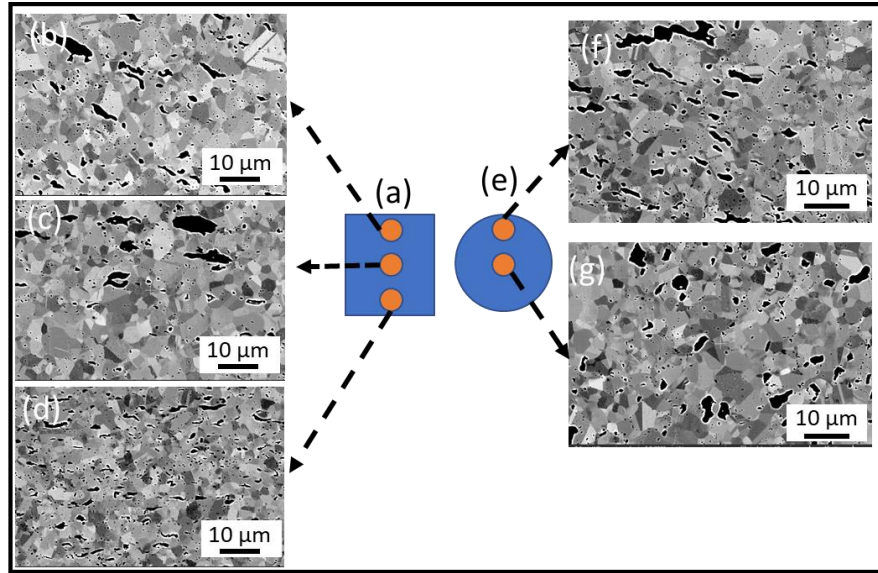


Figure 24. SEM and EDS results of friction extruded Ø 5mm brass+graphite rod LFB 9. (a) and (e) show the schematic of regions on the longitudinal and transverse section respectively for SEM imaging. (b)-(d) SEM microstructure from longitudinal section. (f)-(g) SEM from transverse section.

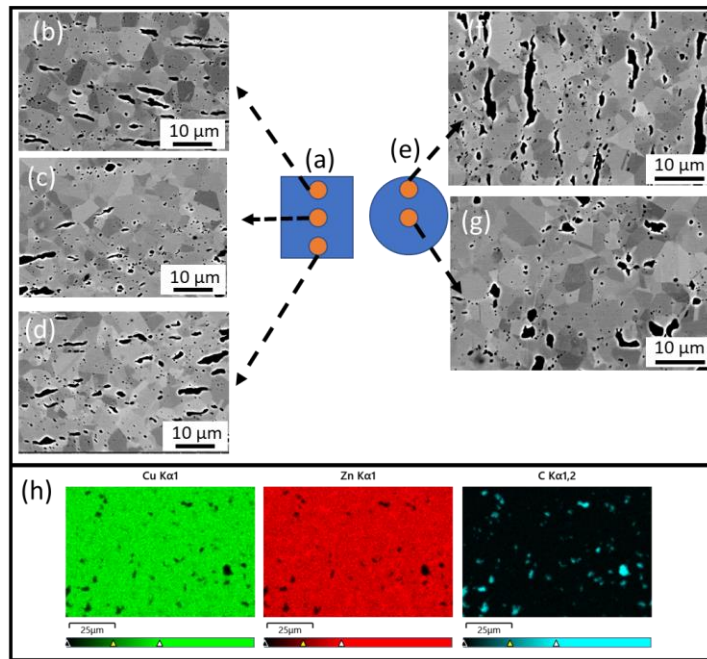


Figure 25: SEM and EDS results of friction extruded Ø 5mm brass+graphite rod LFB 13. (a) and (e) show the schematic of regions on the longitudinal and transverse section respectively for SEM imaging. (b)-(d) SEM microstructure from longitudinal section. (f)-(g) SEM from transverse section. (h) EDS results showing homogenous distribution of Cu and Zn with added carbon distributed throughout.

Pacific Northwest National Laboratory

902 Battelle Boulevard
P.O. Box 999
Richland, WA 99354

1-888-375-PNNL (7665)

www.pnnl.gov